



# Photothermal synergistic effect of $\text{Ti}_3\text{C}_2\text{T}_x/\text{ZnIn}_2\text{S}_4$ Schottky junction for efficient inactivation of antibiotic-resistant bacteria and genes: Mechanism discussion and practical application

Mingmei Li<sup>a,1</sup>, Kaida Zhang<sup>a,1</sup>, Pengfei Wang<sup>a</sup>, Zhiruo Zhou<sup>b</sup>, Fei Li<sup>a</sup>, Sihui Zhan<sup>a,\*</sup>, Yi Li<sup>c,\*</sup>

<sup>a</sup> MOE Key Laboratory of Pollution Processes and Environmental Criteria, Tianjin Key Laboratory of Environmental Remediation and Pollution Control, College of Environmental Science and Engineering, Nankai University, Tianjin 300350, China

<sup>b</sup> School of Environmental Science and Engineering, Zhejiang Gongshang University, Hangzhou 310012, China

<sup>c</sup> Department of Chemistry, Tianjin University, Tianjin 300072, China

## ARTICLE INFO

### Keywords:

Photothermal synergistic effect  
Schottky junction  
Antibiotic-resistant bacteria  
Antibiotic-resistant genes  
Secondary effluent

## ABSTRACT

Antibiotic-resistant bacteria (ARB) and antibiotic-resistant genes (ARGs) in wastewater pose a significant threat to public health. Photothermal synergistic catalysis has the great potential to effectively mitigate ARB and ARG pollution. Herein, we design a  $\text{Ti}_3\text{C}_2\text{T}_x/\text{ZnIn}_2\text{S}_4$  ( $\text{Ti}_3\text{C}_2\text{T}_x/\text{ZIS}$ ) Schottky junction with photothermal effect by exploiting the contact potential difference between  $\text{Ti}_3\text{C}_2\text{T}_x$  and  $\text{ZnIn}_2\text{S}_4$ . The experimental results and DFT calculations demonstrate that the Schottky barrier inhibits electron backflow, thereby enhancing the photodynamic properties of  $\text{Ti}_3\text{C}_2\text{T}_x/\text{ZIS}$ . The photothermal heating effect, induced by the localized surface plasmon resonance (LSPR) of  $\text{Ti}_3\text{C}_2\text{T}_x$ , further enhances ROS production via facilitating charge transfer. Profiting from the photothermal synergistic effect,  $\text{Ti}_3\text{C}_2\text{T}_x/\text{ZIS}$  can completely inactivate ARB within 25 min and degrade 5-log ARG within 120 min under vis-NIR light irradiation. The  $\text{Ti}_3\text{C}_2\text{T}_x/\text{ZIS}$  demonstrated its potential for practical wastewater treatment in a flow-through reactor process, achieving 4-log bacteria inactivation and 99.7% ARG removal from secondary effluent after continuous operation for 8 h.

## 1. Introduction

With the abuse of antibiotics, the propagation of antibiotic-resistant bacteria (ARB) and antibiotic-resistant genes (ARGs) has become a global problem, posing serious threat to ecological environment security and human health [1,2]. It is reported that the outbreak of COVID-19 has intensified the spread of ARB and ARG through sewage disposal plants [3–5]. However, traditional sterilization techniques such as chlorination and ozonation are inadequate in completely inactivating ARB and ARGs, while also presenting drawbacks including high costs, potential regrowth, and by-product generation [6,7]. Photocatalysis is a potential disinfection approach due to its low side-effects, energy saving and low cost [8]. However, the practical application of photocatalysis is hindered by low light utilization efficiency, poor charge migration efficiency, and rapid electron-hole recombination [9].

Photothermal process driven by solar energy can accelerate the separation and migration of photogenerated charges, facilitating the

formation of reactive oxygen species (ROS) [10,11]. In addition, it is reported that the proteins and lipids on the cell membrane could be destroyed when the bacteria are exposed to sub-boiling temperatures (55–60 °C) [12,13]. Therefore, photothermal synergistic catalysis, which combines photocatalysis and thermal catalysis, has great potential in practical wastewater disinfection as it can improve sterilization efficiency by releasing ROS and generating high local temperature [14,15].

Plasmonic nanomaterials, such as noble-metal-based materials, are one of the earliest photothermal catalysts [16,17]. However, the practical application of these plasmonic metals is restricted by their high cost and/or cytotoxicity [13,18]. As a representative member of MXene,  $\text{Ti}_3\text{C}_2\text{T}_x$  ( $\text{T}_x$  stands for surface functional group) is an attractive and environmentally friendly photothermal material due to its local surface plasmon resonance (LSPR) effect, high absorption and conversion efficiencies for Vis-NIR light and excellent conductivity [11,19].  $\text{Ti}_3\text{C}_2\text{T}_x$  exhibits a stronger photothermal effect in the NIR region compared to

\* Corresponding authors.

E-mail addresses: [sihuizhan@nankai.edu.cn](mailto:sihuizhan@nankai.edu.cn) (S. Zhan), [liyi@tju.edu.cn](mailto:liyi@tju.edu.cn) (Y. Li).

<sup>1</sup> These authors contributed equally to this work.

plasma metals due to the slower relaxation of its  $e_{\text{hot}}$  generation [20,21]. The advantages of  $\text{Ti}_3\text{C}_2\text{T}_x$  over traditional plasmonic metals make it a highly promising candidate for water disinfection applications [22,23]. However, the antibacterial activity of  $\text{Ti}_3\text{C}_2\text{T}_x$  alone is insufficient due to its limited photodynamic effect. The combination of  $\text{Ti}_3\text{C}_2\text{T}_x$  and semiconductors is anticipated to yield enhanced photodynamic and photothermal properties [24–26].

In recent years, a wide range of light-responsive semiconductors have been developed such as metallic oxides, polymers, and metal sulfides. Among these reported photocatalysts, ultrathin  $\text{ZnIn}_2\text{S}_4$  (ZIS), a ternary metal sulfide, has garnered significant attention and found numerous applications due to its notable advantages such as facile synthesis methods, cost-effectiveness, environmental friendliness, excellent stability, distinctive adjustable electronic structure, and appropriate band structure [27,28]. Moreover, considering the intrinsic physical properties of  $\text{Ti}_3\text{C}_2\text{T}_x$  and  $\text{ZnIn}_2\text{S}_4$ , which possess different work function (WF) values, we propose that an interfacial self-driven charge transfer channel could be established by combining  $\text{Ti}_3\text{C}_2\text{T}_x$  with  $\text{ZnIn}_2\text{S}_4$  to construct a Schottky junction. This would facilitate efficient charge transfer at the interface, thereby achieving exceptional photodynamic and photothermal properties.

Based on this hypothesis,  $\text{ZnIn}_2\text{S}_4$  nanosheets were grown in situ on the surface of  $\text{Ti}_3\text{C}_2\text{T}_x$  nanosheets ( $\text{Ti}_3\text{C}_2\text{T}_x/\text{ZIS}$ ) for inactivation of ARBs and ARGs under Vis-NIR light irradiation. Our findings disclosed the photothermal synergistic catalytic sterilization mechanism of  $\text{Ti}_3\text{C}_2\text{T}_x/\text{ZIS}$  Schottky junction under Vis-NIR light irradiation: (i) the combination of  $\text{Ti}_3\text{C}_2\text{T}_x$  and  $\text{ZnIn}_2\text{S}_4$  enhanced the photodynamic performance by suppressing recombination of photoinduced charges due to contact potential difference between the two components with different WF values; (ii) the photothermal heating effect induced by the LSPR of  $\text{Ti}_3\text{C}_2\text{T}_x$  further boosted the yield of ROS by promoting the transfer of photogenerated carriers.

## 2. Experimental section

### 2.1. Catalyst preparation

The procedures for catalyst preparation were presented in Text S1.

### 2.2. Detection of ROS

Ascorbic acid (AsA, 50 mg/L) was used to evaluate the ROS generation property of catalysts under Vis-NIR ( $\geq 420$  nm) light irradiation, as it can be oxidized by ROS. The light source was provided by a 300 W Xenon arc lamp (CEL-HXF300) with a UV cutoff ( $\lambda < 420$  nm). The AsA can be quantified using a colorimetric method with an ultraviolet spectrophotometer (the absorbance around 534 nm). Besides, the electron spin resonance (ESR) spectra were recorded on a Bruker-A200 spectrometer (Germany) under Vis-NIR ( $\geq 420$  nm) light irradiation. The concentration of  $\text{H}_2\text{O}_2$  was determined by iodometry. According to previous reports, nitroblue tetrazolium (NBT), terephthalic acid and 9,10-diphenylanthracene (DPA) were employed as probes for the quantification of  $\text{O}_2^{\bullet-}$ ,  $\bullet\text{OH}$  and  $^1\text{O}_2$  concentrations respectively [29,30].

### 2.3. Measurement of photothermal effect

The temperatures of the solid powder material and catalyst solution were recorded using a thermal imager. The temperature evolution of catalysts in the solution was measured under identical conditions to those employed in the photothermal catalytic disinfection experiment. Also,  $\text{Ti}_3\text{C}_2\text{T}_x/\text{ZIS}$ -6 was irradiated under the same condition for 30 min and then cooled in the dark for 30 min.

### 2.4. Disinfection experiments

*E. coli* HB101 was selected as the model ARB to evaluate the

sterilization performance of the samples. The light source is the same as that in the ROS measurement. The detailed procedure of ARB culture and disinfection was shown in Text S3.

### 2.5. ARGs Removal Tests

The amplicons of *tetA* (tetracycline resistance genes), *ampC* ( $\beta$ -Lactam resistance genes) and *sul2* (sulfanilamide resistance genes) were selected as the target model. The removal tests of ARGs by catalysts were carried out in a beaker at  $25 \pm 0.2$  °C with an initial solution pH of  $\sim 7$ . The light source is the same as that in the ROS measurement. The details of extraction, degradation and analysis were detailed in Text S4.

### 2.6. Theoretical calculation

In density functional theory (DFT) calculation, structural optimization was performed by Vienna Ab-initio Simulation Package (VASP) [31] with the projector augmented wave (PAW) method [32]. The exchange-functional was treated using the Perdew-Burke-Ernzerhof (PBE) [33] functional in combination with the DFT-D3 correction [34], to describe the weak interactions between atoms. For the optimization of both geometry and lattice size, the Brillouin zone integration was performed with  $3 \times 3 \times 1$  Monkhorst-Pack *k*-point sampling [35]. The equilibrium geometries and lattice constants were optimized with maximum stress on each atom within  $0.02 \text{ eV } \text{\AA}^{-3}$ . Isosurface level of charge density difference was set at  $0.001 \text{ e } \text{\AA}^{-3}$ . Work function of  $\text{Ti}_3\text{C}_2\text{O}_2/\text{ZnIn}_2\text{S}_4$  heterostructure was obtained by vaspkit interface [36].

## 3. Results and discussion

### 3.1. Preparation and characterization of $\text{Ti}_3\text{C}_2\text{T}_x/\text{ZIS}$ Schottky catalyst

Fig. 1a exhibited the preparation process of  $\text{Ti}_3\text{C}_2\text{T}_x/\text{ZIS}$  heterostructure and the corresponding material structures at different synthesis stages. The bulk  $\text{Ti}_3\text{AlC}_2$  was etched by the mixed solution of HCl and LiF to obtain the multilayer  $\text{Ti}_3\text{C}_2\text{T}_x$ . After ultrasonic exfoliation, few-layer  $\text{Ti}_3\text{C}_2\text{T}_x$  nanosheets can be prepared (Fig. 1b and Fig. S1). Under solvothermal conditions, ultra-thin  $\text{ZnIn}_2\text{S}_4$  nanosheets can uniformly grow on the surface of  $\text{Ti}_3\text{C}_2\text{T}_x$  to form  $\text{Ti}_3\text{C}_2\text{T}_x/\text{ZnIn}_2\text{S}_4$  heterostructure ( $\text{Ti}_3\text{C}_2\text{T}_x/\text{ZIS}$ ). The flower-like  $\text{ZnIn}_2\text{S}_4$  was also synthesized as the control sample (Fig. 1c and Fig. S2). The transmission electron microscopy (TEM) image of  $\text{Ti}_3\text{C}_2\text{T}_x/\text{ZIS}$  (Fig. 1d) indicated that the  $\text{ZnIn}_2\text{S}_4$  was tightly anchored on  $\text{Ti}_3\text{C}_2\text{T}_x$  nanosheets to ensure close contact. The high-resolution TEM (HRTEM) result (Fig. 1e) exhibited lattices of 0.26 and 0.19 nm, corresponding to the (0110) crystal plane of  $\text{Ti}_3\text{C}_2\text{T}_x$  and the (110) crystal plane of  $\text{ZnIn}_2\text{S}_4$  [37], suggesting the successful synthesis of heterojunction catalysts. The corresponding TEM elemental mappings showed that the Zn, In, S, Ti and C elements were uniformly distributed across the composite (Fig. 1f).

The X-ray diffraction (XRD) patterns of  $\text{ZnIn}_2\text{S}_4$  and  $\text{Ti}_3\text{C}_2\text{T}_x/\text{ZIS}$  with different contents of  $\text{Ti}_3\text{C}_2\text{T}_x$  (Fig. 2a and Fig. S3) can be indexed to the hexagonal phase of  $\text{ZnIn}_2\text{S}_4$  (JCPDS No. 65–2023), indicating their high purity without any crystal alteration. The tiny peaks observed at about  $7^\circ$  and  $61^\circ$  in the  $\text{Ti}_3\text{C}_2\text{T}_x/\text{ZIS}$  sample can be attributed to the (002) and (110) crystal faces of  $\text{Ti}_3\text{C}_2\text{T}_x$  [11,38]. The signals of Ti, C, O, Zn, In and S were detected in  $\text{Ti}_3\text{C}_2\text{T}_x/\text{ZIS}$ -6 by X-ray photoelectron spectroscopy (XPS) survey scan (Fig. S4a), which was consistent with the results obtained from TEM energy-dispersive X-ray spectra (TEM-EDX) (Fig. S5), indicating the successful combination of  $\text{Ti}_3\text{C}_2\text{T}_x$  and  $\text{ZnIn}_2\text{S}_4$ . The actual contents of  $\text{Ti}_3\text{C}_2\text{T}_x$  in  $\text{Ti}_3\text{C}_2\text{T}_x/\text{ZIS}$ -6 was calculated to be 5.42 wt% by inductively coupled plasma mass spectrometry (ICP-MS) (Table S3). Due to the low content of  $\text{Ti}_3\text{C}_2\text{T}_x$  and the superposition of In 3d and Ti 2p, only a weak Ti 2p peak can be detected in the XPS spectrum (Fig. 2b). The significant decrease of the F peak observed in the F 1s spectrum of  $\text{Ti}_3\text{C}_2\text{T}_x/\text{ZIS}$ -6 suggested that the F functional group on the surface of

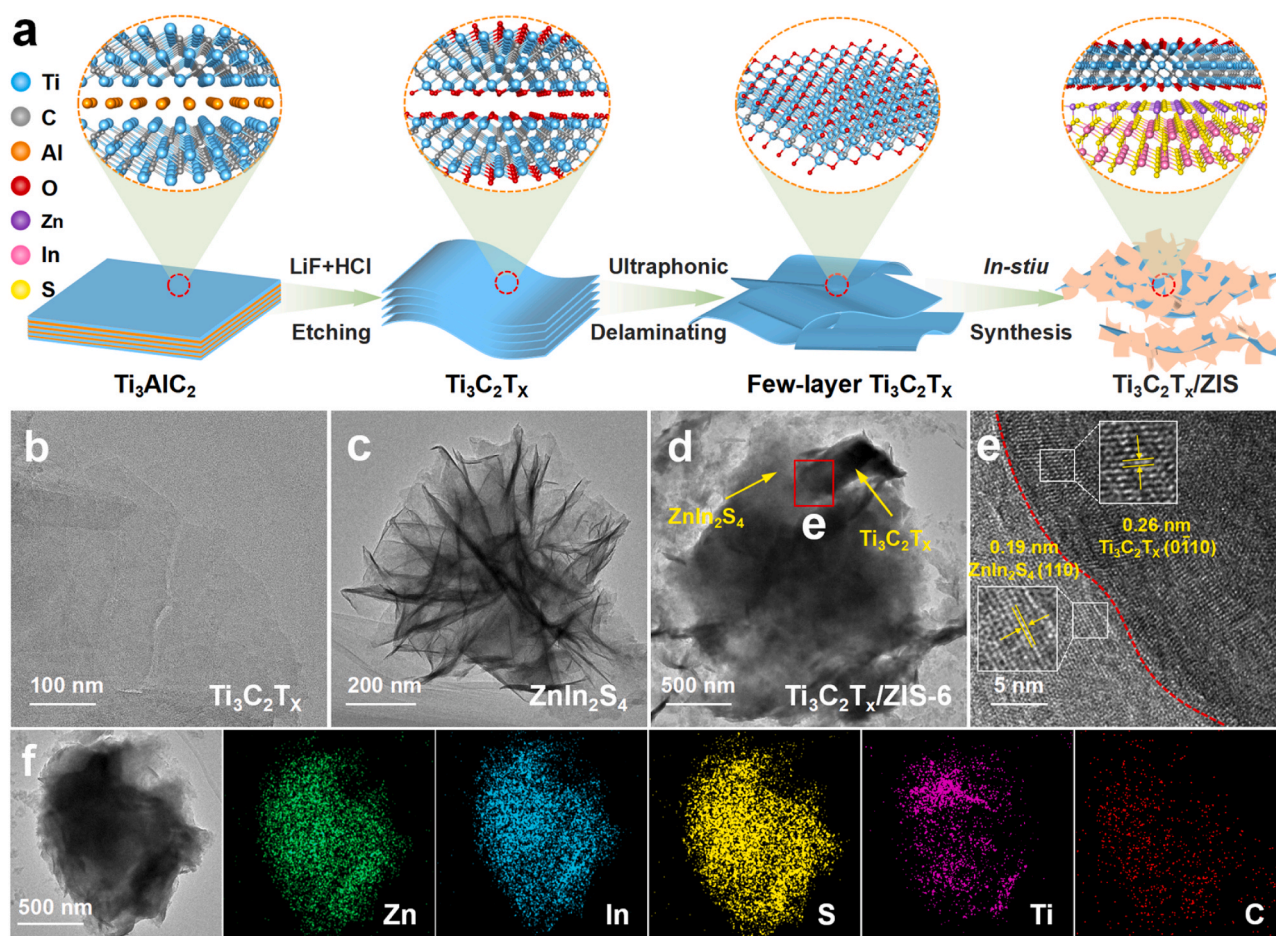


**Fig. 1.** (a) Schematic illustration of the synthesis procedure. TEM images of (b)  $\text{Ti}_3\text{C}_2\text{T}_x$ , (c)  $\text{ZnIn}_2\text{S}_4$  and (d)  $\text{Ti}_3\text{C}_2\text{T}_x/\text{ZIS-6}$ . (e) HRTEM image and (f) EDS elemental mappings of  $\text{Ti}_3\text{C}_2\text{T}_x/\text{ZIS-6}$ .

$\text{Ti}_3\text{C}_2\text{T}_x$  was lost during the solvothermal process (Fig. 2c). Besides, the ratio between the -OH: -O functional group was 0.31: 1 in  $\text{Ti}_3\text{C}_2\text{T}_x/\text{ZIS-6}$ , indicating that the main functional group in  $\text{Ti}_3\text{C}_2\text{T}_x/\text{ZIS-6}$  was -O (Fig. S4c). Notably, the C-Ti peak of  $\text{Ti}_3\text{C}_2\text{T}_x/\text{ZIS}$  exhibited a shift towards lower binding energy in comparison to that of  $\text{Ti}_3\text{C}_2\text{T}_x$  (Fig. 2d), while its Zn 2p shifted to higher binding energy compared to that of  $\text{ZnIn}_2\text{S}_4$  (Fig. 2e). The results confirmed the strong interface interaction between  $\text{Ti}_3\text{C}_2\text{T}_x$  and  $\text{ZnIn}_2\text{S}_4$ , leading to a reduction in the local electron density of Zn centers and an increase in that of C centers. This resulted in electrons transferring from  $\text{ZnIn}_2\text{S}_4$  to  $\text{Ti}_3\text{C}_2\text{T}_x$  when they are tightly contacted [11,39]. Moreover, the structure of  $\text{Ti}_3\text{C}_2\text{T}_x/\text{ZIS-6}$  was analyzed by Raman spectra (Fig. 2f). The peaks at  $600\text{ cm}^{-1}$ ,  $1401\text{ cm}^{-1}$  and  $1564\text{ cm}^{-1}$  can be attributed to the stretching modes of  $\text{ZnIn}_2\text{S}_4$ , D and G bands of  $\text{Ti}_3\text{C}_2\text{T}_x$ , respectively [37,40]. The increased  $I_D/I_G$  value of  $\text{Ti}_3\text{C}_2\text{T}_x/\text{ZIS-6}$  further confirmed the robust interaction and efficient electron transfer between  $\text{Ti}_3\text{C}_2\text{T}_x$  and  $\text{ZnIn}_2\text{S}_4$  [41]. Consequently, a Schottky junction and built-in electric field were established at the interface between  $\text{Ti}_3\text{C}_2\text{T}_x$  and  $\text{ZnIn}_2\text{S}_4$ .

### 3.2. Photocatalytic and photothermal performance

The yield of ROS reflects the catalytic reaction activity of catalysts. Therefore, the ROS generated by the catalysts under Vis-NIR light irradiation were detected using ascorbic acid (AsA) as an indicator molecule [11]. As shown in Fig. 3a, the AsA removal efficiency of  $\text{Ti}_3\text{C}_2\text{T}_x/\text{ZIS}$  samples were much higher than that of pure  $\text{Ti}_3\text{C}_2\text{T}_x$  and  $\text{ZnIn}_2\text{S}_4$ , and  $\text{Ti}_3\text{C}_2\text{T}_x/\text{ZIS-6}$  reaching the highest value. Thus,  $\text{Ti}_3\text{C}_2\text{T}_x/\text{ZIS-6}$  possessed the best Vis-NIR photocatalytic activity. The ROS type generated during

the photocatalytic process was identified through ESR trapping tests. As exhibited in Fig. 3b-d, the signals of  $\bullet\text{OH}$ ,  $\text{O}_2^{\bullet-}$ ,  $^1\text{O}_2$  were detected in  $\text{ZnIn}_2\text{S}_4$  and  $\text{Ti}_3\text{C}_2\text{T}_x/\text{ZIS-6}$  systems, while no signals of these four species were detected in the  $\text{Ti}_3\text{C}_2\text{T}_x$  system, demonstrating that both  $\text{ZnIn}_2\text{S}_4$  and  $\text{Ti}_3\text{C}_2\text{T}_x/\text{ZIS-6}$  can generate  $\bullet\text{OH}$ ,  $\text{O}_2^{\bullet-}$  and  $^1\text{O}_2$  under Vis-NIR light irradiation. In addition, the concentration of ROS generated during the photocatalytic process was quantified using colorimetric techniques. As shown in Fig. 3e-h, the concentrations of  $\text{H}_2\text{O}_2$ ,  $\bullet\text{OH}$ ,  $\text{O}_2^{\bullet-}$  and  $^1\text{O}_2$  in the  $\text{Ti}_3\text{C}_2\text{T}_x/\text{ZIS-6}$  photocatalytic system were detected as  $3.95 \times 10^{-5}$ ,  $2.93 \times 10^{-5}$ ,  $1.01 \times 10^{-5}$  and  $0.93 \times 10^{-5}$  mol/L within a period of 60 min. It is noteworthy that the concentration of  $\text{H}_2\text{O}_2$  in the  $\text{Ti}_3\text{C}_2\text{T}_x/\text{ZIS-6}$  system surpassed that of  $\bullet\text{OH}$ ,  $\text{O}_2^{\bullet-}$  and  $^1\text{O}_2$ , indicating that  $\text{H}_2\text{O}_2$  was the primary active species generated by  $\text{Ti}_3\text{C}_2\text{T}_x/\text{ZIS-6}$  under Vis-NIR irradiation. The concentration of  $\text{O}_2^{\bullet-}$  in the  $\text{Ti}_3\text{C}_2\text{T}_x/\text{ZIS-6}$  system was slightly lower compared to that in the  $\text{ZnIn}_2\text{S}_4$  system, potentially attributed to the reduction of Fermi level caused by the introduction of  $\text{Ti}_3\text{C}_2\text{T}_x$  into  $\text{ZnIn}_2\text{S}_4$ , resulting in a diminished capacity of photogenerated electrons for oxidizing  $\text{O}_2$  to  $\text{O}_2^{\bullet-}$ . However, the concentrations of  $\text{H}_2\text{O}_2$ ,  $\bullet\text{OH}$ , and  $^1\text{O}_2$  in the  $\text{Ti}_3\text{C}_2\text{T}_x/\text{ZIS-6}$  photocatalytic system were significantly higher compared to those in both the  $\text{Ti}_3\text{C}_2\text{T}_x$  and  $\text{ZnIn}_2\text{S}_4$  photocatalytic systems, indicating that the introduction of  $\text{Ti}_3\text{C}_2\text{T}_x$  promoted the generation of ROS. According to the above results,  $\text{Ti}_3\text{C}_2\text{T}_x/\text{ZIS-6}$  exhibited excellent Vis-NIR photocatalytic photocatalytic reaction activity.

The photocatalytic and photothermal performance of the prepared materials were assessed because of their intimate correlation with the production of ROS [23]. The photocatalytic performance the samples under Vis-NIR light irradiation was analyzed through photochemical



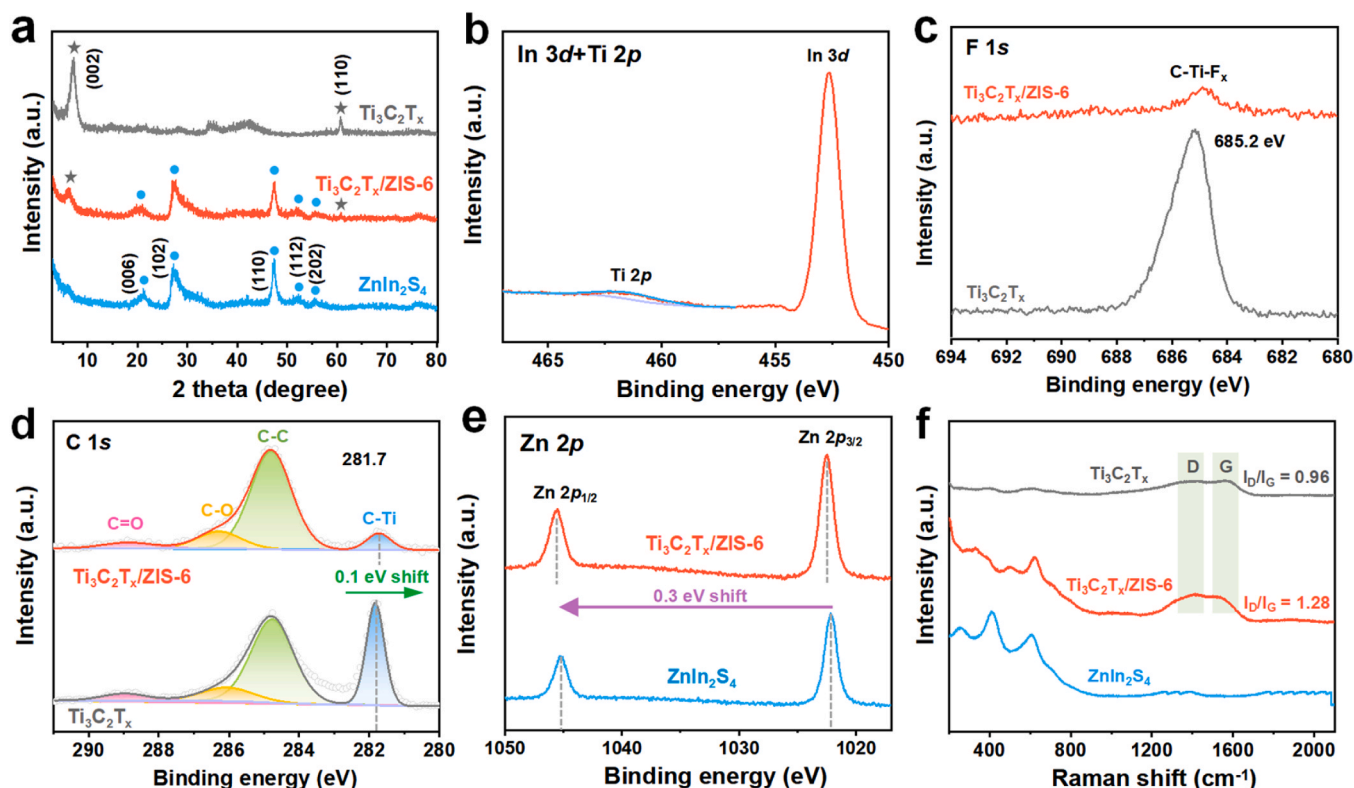


**Fig. 2.** (a) XRD pattern. The high-resolution XPS spectra of the prepared samples: (b) In 3d + Ti 2p, (c) F 1s, (d) C 1s and (e) Zn 2p. (f) Raman spectra of the prepared samples.

and photoelectrochemical measurements. UV-Vis-NIR diffuse reflectance spectra (Fig. 4a) showed that  $\text{Ti}_3\text{C}_2\text{T}_\text{x}/\text{ZIS-6}$  exhibited superior Vis-NIR-light-harvesting capability compared to  $\text{ZnIn}_2\text{S}_4$ , which can be attributed to the full spectrum absorption of  $\text{Ti}_3\text{C}_2\text{T}_\text{x}$  and its unique layered branching structure [37,42]. Furthermore, the separation efficiency of electron-hole pairs and the lifetime of photo-induced charges were investigated by photoluminescence (PL) measurements. As exhibited in steady-state PL spectra (Fig. 4b and Fig. S6), the peak of  $\text{ZnIn}_2\text{S}_4$  at 583.1 nm was attributed to the direct band transition. However, the emission peaks in the PL spectra of  $\text{Ti}_3\text{C}_2\text{T}_\text{x}/\text{ZIS}$  samples shifted towards longer wavelengths, indicating that the introduction of  $\text{Ti}_3\text{C}_2\text{T}_\text{x}$  resulted in the formation of impurity levels within  $\text{ZnIn}_2\text{S}_4$ 's band gap [43]. Besides, both the PL intensity of  $\text{Ti}_3\text{C}_2\text{T}_\text{x}/\text{ZIS}$  composites was lower than that of  $\text{ZnIn}_2\text{S}_4$ , suggesting the inhibited recombination of  $\text{e}^-$  and  $\text{h}^+$  in  $\text{Ti}_3\text{C}_2\text{T}_\text{x}/\text{ZIS}$  heterojunction [44]. In the time-resolved PL spectra (Fig. 4c and Fig. S7),  $\text{Ti}_3\text{C}_2\text{T}_\text{x}/\text{ZIS-6}$  exhibited the longest charge carrier lifetime (5.80 ns) compared to  $\text{ZnIn}_2\text{S}_4$  (3.45 ns) and  $\text{Ti}_3\text{C}_2\text{T}_\text{x}$  (1.26 ns), indicating that more photoexcited charges participated in the photocatalytic reaction to generate more ROS in the  $\text{Ti}_3\text{C}_2\text{T}_\text{x}/\text{ZIS-6}$  photocatalytic system. Moreover, based on the Mott-Schottky curves (Fig. 4d),  $\text{Ti}_3\text{C}_2\text{T}_\text{x}/\text{ZIS-6}$  exhibited a carrier density of  $1.14 \times 10^{22} \text{ cm}^{-3}$ , which was approximately  $3.86 \times 10^5$  times higher than that of  $\text{ZnIn}_2\text{S}_4$  ( $2.95 \times 10^{16} \text{ cm}^{-3}$ ). This provided further evidence for the facilitation of electron transfer in the  $\text{Ti}_3\text{C}_2\text{T}_\text{x}/\text{ZIS-6}$  heterojunction. Additionally, the electrochemical impedance spectroscopy (EIS) test was performed to determine the charge migration resistance in the catalysts (Fig. 4e). The interface charge transfer resistance values of  $\text{ZnIn}_2\text{S}_4$  ( $2.2 \times 10^6 \Omega$ ) and  $\text{Ti}_3\text{C}_2\text{T}_\text{x}$  ( $7.8 \times 10^4 \Omega$ ) were found to be 137.5 times and 4.8 times higher than that of  $\text{Ti}_3\text{C}_2\text{T}_\text{x}/\text{ZIS-6}$  ( $1.6 \times 10^4 \Omega$ ), respectively, indicating that the  $\text{Ti}_3\text{C}_2\text{T}_\text{x}/\text{ZIS-6}$  Schottky catalyst possesses a high-speed channel for efficient migration and separation of photogenerated charge carriers.

To further verify the solar-driven photothermal synergism catalysis, the photothermal conversion performance of catalysts was studied. Under Vis-NIR light ( $\geq 420 \text{ nm}$ ) irradiation, the temperature of  $\text{Ti}_3\text{C}_2\text{T}_\text{x}/$

ZIS-6 solid reached approximately  $324.7^\circ \text{C}$  within 10 min (Fig. S8), and the temperature of  $\text{Ti}_3\text{C}_2\text{T}_\text{x}/\text{ZIS-6}$  solution reached about  $55^\circ \text{C}$  within 30 min (Fig. 4f, S9-S10). The repeatable heating/cooling curve indicated that the synthesized  $\text{Ti}_3\text{C}_2\text{T}_\text{x}/\text{ZIS}$  showed satisfactory photothermal stability without obvious temperature change even after four illumination cycles (Fig. 4g). These results demonstrated that the  $\text{Ti}_3\text{C}_2\text{T}_\text{x}/\text{ZIS}$  Schottky junction can effectively convert light energy into thermal energy. Given that elevated temperatures can accelerate the separation and transfer of photogenerated charges, potentially promoting the generation of ROS [23,45], we evaluated the contribution of photothermal heating to increased ROS yield. The negligible steady-state temperature difference ( $< 8.33 \times 10^{-4} \text{ K}$ ) observed at the  $\text{Ti}_3\text{C}_2\text{T}_\text{x}/\text{ZIS-6}$ -water interface (Test S6) indicated that precise temperature control can effectively eliminate the impact of thermochemical catalysis. The reduced photocurrent density of  $\text{Ti}_3\text{C}_2\text{T}_\text{x}/\text{ZIS-6}$  at  $25^\circ \text{C}$  proved the promoting effect of photothermal heating on the transfer of photoinduced carriers (Fig. 4h). Compared to the control group without temperature regulation,  $\text{Ti}_3\text{C}_2\text{T}_\text{x}/\text{ZIS-6}$  exhibited an approximately 40% reduction in oxidation efficiency towards AsA at  $25^\circ \text{C}$  (Fig. 4i), indicating that the synergistic photodynamic and photothermal effects facilitated ROS production.

### 3.3. Mechanism of photocatalytic performance

Based on the band theory, the WF of  $\text{Ti}_3\text{C}_2\text{T}_\text{x}$  and  $\text{ZnIn}_2\text{S}_4$  may exert an influence on electron migration behavior. The WF values of the prepared catalysts can be obtained by subtracting the excitation energy of He I from the secondary electron cutoff energy ( $E_{\text{cutoff}}$ ) measured via ultraviolet photoelectron spectroscopy (UPS). As depicted in Fig. 5a, the  $E_{\text{cutoff}}$  values of  $\text{ZnIn}_2\text{S}_4$ ,  $\text{Ti}_3\text{C}_2\text{T}_\text{x}$  and  $\text{Ti}_3\text{C}_2\text{T}_\text{x}/\text{ZIS-6}$  were 17.16 eV, 16.90 eV and 16.94 eV, respectively, thus the corresponding WF were determined to be 4.06 eV, 4.32 eV and 4.28 eV, respectively. The theoretical WF value of  $\text{Ti}_3\text{C}_2\text{T}_\text{x}/\text{ZIS-6}$  (4.49 eV) calculated by density function theory (DFT) calculation (Fig. 5b) was in excellent agreement



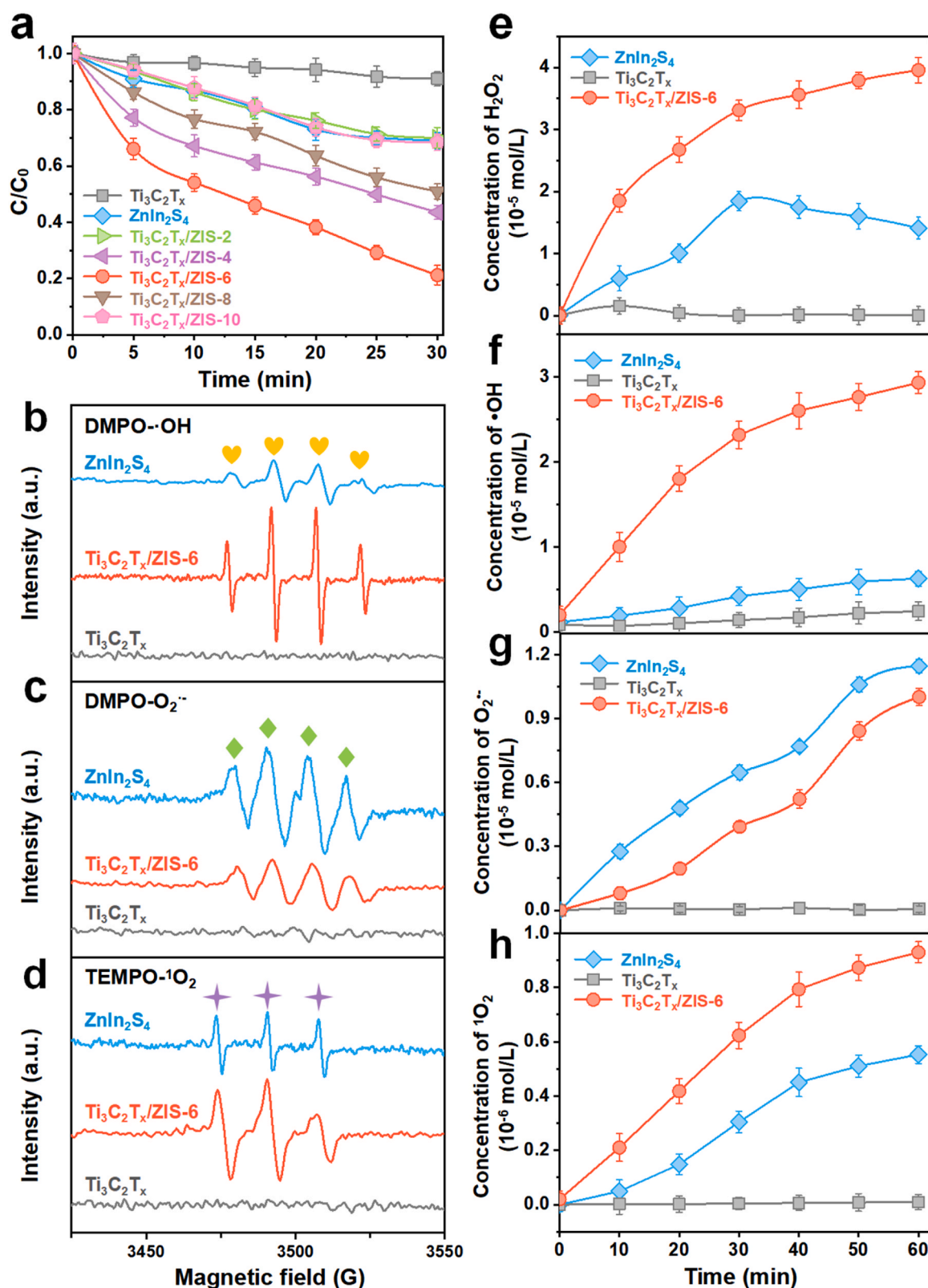


**Fig. 3.** (a) AsA oxidation efficiency during a 30-min photocatalytic test by the prepared samples (100 mg/L). (b) ESR spectra of the samples (b) in  $\text{H}_2\text{O}$  (detect the •OH) and (c) methanol (detect the  $\text{O}_2^{\bullet-}$ ) with DMPO as a radical trapper. (d) ESR spectra of the samples in  $\text{H}_2\text{O}$  with TEMP as a radical trapper (detect the  $^1\text{O}_2$ ). Concentration of (e)  $\text{H}_2\text{O}_2$ , (f) •OH, (g)  $\text{O}_2^{\bullet-}$  and (h)  $^1\text{O}_2$  were determined during the photocatalytic process under Vis-NIR light irradiation.

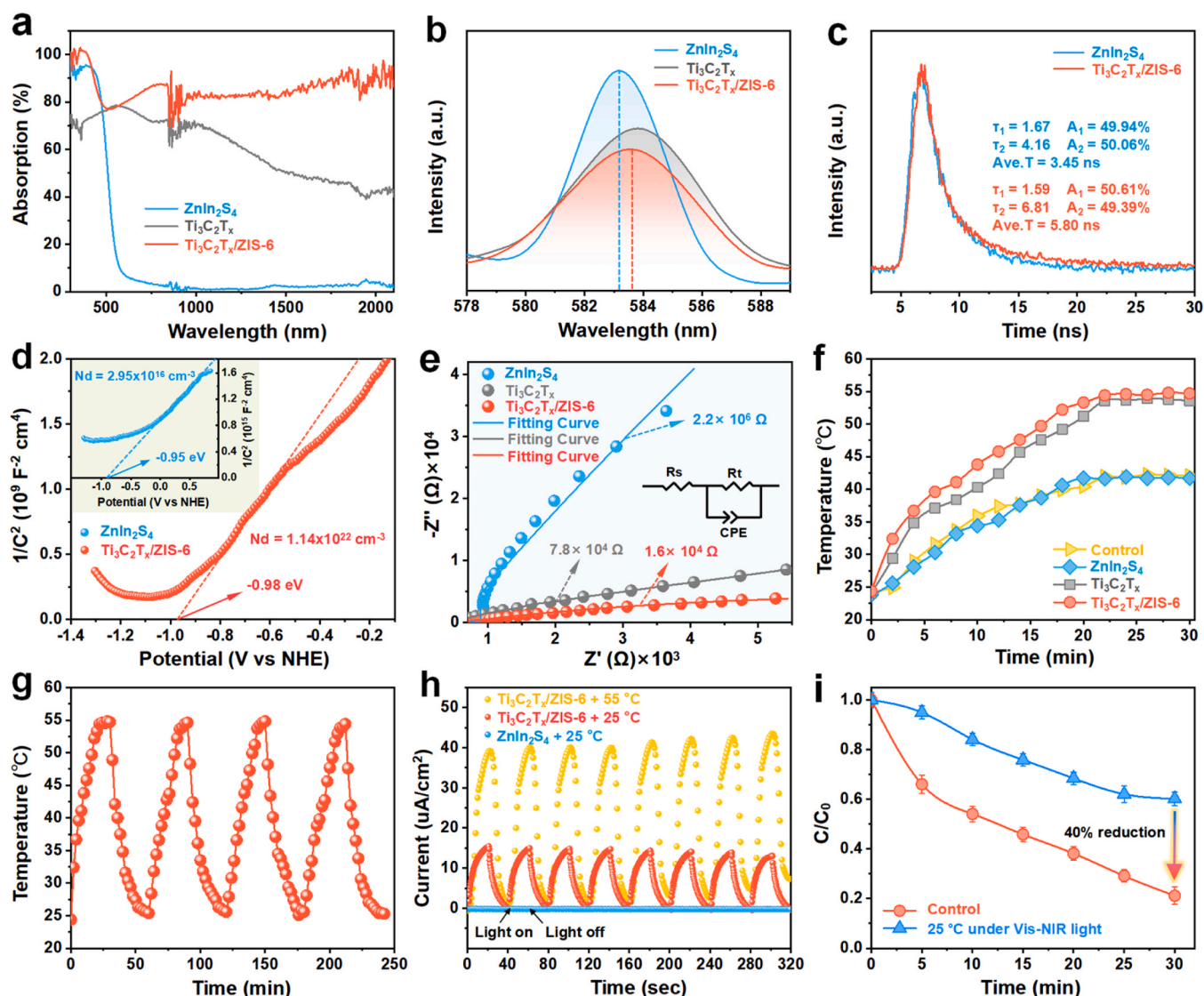


**Fig. 4.** (a) UV-Vis-NIR diffuse reflectance spectra. (b) Steady-state PL spectra, (c) time-resolved PL spectra, (d) Mott-Schottky plots and (e) EIS Nyquist plots of the prepared samples. (f) Photothermal curves of different catalyst solutions (100 mg/L) under Vis-NIR light irradiation. (g) Temperature rising and cooling profiles of  $\text{Ti}_3\text{C}_2\text{T}_x/\text{ZIS-6}$  solution when the irradiation is on/off under Vis-NIR light. (h) Photocurrent responses. (i) The AsA oxidation efficiency of  $\text{Ti}_3\text{C}_2\text{T}_x/\text{ZIS-6}$  under different treatment conditions.

with the UPS result. The valence band top (VB) of  $\text{ZnIn}_2\text{S}_4$  and  $\text{Ti}_3\text{C}_2\text{T}_x/\text{ZIS-6}$ , as determined by XPS valence spectra, were found to be approximately 1.57 eV and 1.53 eV, respectively (Fig. 5c). Therefore, the calculated valence band energy maximum ( $E_V$ ) for  $\text{ZnIn}_2\text{S}_4$  and  $\text{Ti}_3\text{C}_2\text{T}_x/\text{ZIS-6}$  were 5.97 eV and 5.93 eV, respectively (vs. absolute vacuum scale). Based on the Tauc's band gap plot analysis, the energy band gap ( $E_g$ ) of  $\text{ZnIn}_2\text{S}_4$  and  $\text{Ti}_3\text{C}_2\text{T}_x/\text{ZIS-6}$  were determined to be 2.35 eV and 2.23 eV, respectively (Fig. S11). Thus, the conduction band energy minimum ( $E_C$ ) of  $\text{ZnIn}_2\text{S}_4$  and  $\text{Ti}_3\text{C}_2\text{T}_x/\text{ZIS-6}$  were 3.62 eV and 3.70 eV, respectively. In theory, a Schottky junction could be formed at the interface between  $\text{ZnIn}_2\text{S}_4$  and  $\text{Ti}_3\text{C}_2\text{T}_x$  due to the higher Fermi level ( $E_F$ ) of  $\text{ZnIn}_2\text{S}_4$  compared to that of  $\text{Ti}_3\text{C}_2\text{T}_x$ . Upon contact between  $\text{ZnIn}_2\text{S}_4$  and  $\text{Ti}_3\text{C}_2\text{T}_x$ , the  $e^-$  spontaneously transferred from  $\text{ZnIn}_2\text{S}_4$  to  $\text{Ti}_3\text{C}_2\text{T}_x$  until equilibrium was achieved. This was confirmed by XPS peak shifts and the calculated electron density distribution (Fig. 5d). In this process, the positively charged layer was formed on the surface of  $\text{ZnIn}_2\text{S}_4$  due to the electron loss, resulting in an upward energy band. Simultaneously, a negatively charged layer was created on the surface of  $\text{Ti}_3\text{C}_2\text{T}_x$ . Therefore, the interface between  $\text{ZnIn}_2\text{S}_4$  and  $\text{Ti}_3\text{C}_2\text{T}_x$  gave rise to the formation of Schottky barrier and built-in electric field [11,46], as

demonstrated in Fig. 5e.

Based on the above analysis, a mechanism for enhancing ROS yield by  $\text{Ti}_3\text{C}_2\text{T}_x/\text{ZIS}$  Schottky heterostructure in Vis-NIR-induced progress was proposed (Fig. 5f). Under Vis-NIR light excitation, the photoinduced  $e^-$  from  $\text{ZnIn}_2\text{S}_4$  jumped into the conduction band and subsequently migrated along the Schottky junction to  $\text{Ti}_3\text{C}_2\text{T}_x$ . The Schottky barrier almost inhibited the backflow of  $e^-$ , thereby enhancing the separation efficiency of photoexcited electron-hole pairs. Meanwhile, the localized surface temperature of  $\text{Ti}_3\text{C}_2\text{T}_x/\text{ZIS}$  was elevated by the photothermal effect induced by LSPR of  $\text{Ti}_3\text{C}_2\text{T}_x$ , which in turn facilitated the transfer of photogenerated carriers and increased free charge concentration. Subsequently, the electrons accumulated on the surface of  $\text{Ti}_3\text{C}_2\text{T}_x$  were captured by surrounding species to generate ROS. Additionally, the intimate contact between  $\text{Ti}_3\text{C}_2\text{T}_x$  and  $\text{ZnIn}_2\text{S}_4$  provided a pathway for photoinduced charges transfer. Consequently, the optimum match of  $\text{Ti}_3\text{C}_2\text{T}_x/\text{ZIS}$  generated more ROS.

### 3.4. Bactericidal performance and mechanism

*E. coli* HB101 was selected as the model to evaluate the disinfection

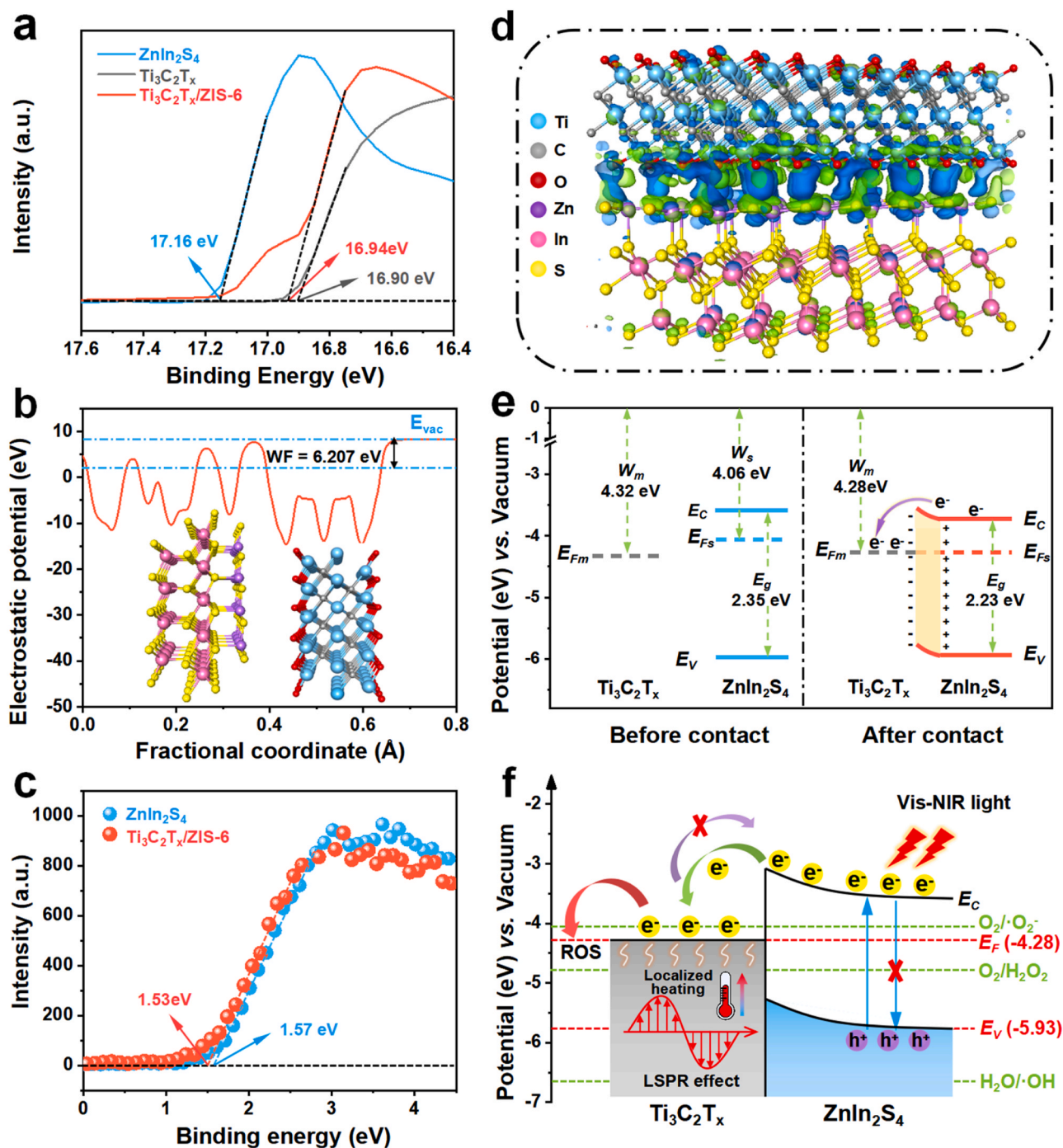


**Fig. 5.** (a) UPS spectra measured by He I ( $h\nu = 21.22$  eV) spectra the secondary electron cutoff. (b) Electrostatic potential of  $\text{Ti}_3\text{C}_2\text{T}_x/\text{ZIS-6}$  along z axis. (c) High-resolution XPS valence band spectra of the prepared samples. (d) Difference charge density of  $\text{Ti}_3\text{C}_2\text{T}_x/\text{ZIS-6}$ . (e) Energy scheme before and after the contact of  $\text{Ti}_3\text{C}_2\text{T}_x$  and  $\text{ZnIn}_2\text{S}_4$ . WF, work function.  $E_g$ , energy gap.  $E_C$ , conduction band minimum,  $E_V$ , valence band maximum. (f) The mechanism for the enhanced the yield of ROS via Vis-NIR-light-induced progress based on the Schottky heterostructure of  $\text{Ti}_3\text{C}_2\text{T}_x/\text{ZIS}$ .

performance of the catalysts. Fig. 6a and S12 demonstrated the bactericidal activity of  $\text{Ti}_3\text{C}_2\text{T}_x/\text{ZIS}$  composites with varying  $\text{Ti}_3\text{C}_2\text{T}_x$  contents, among which  $\text{Ti}_3\text{C}_2\text{T}_x/\text{ZIS-6}$  exhibited the most potent sterilization activity. Therefore,  $\text{Ti}_3\text{C}_2\text{T}_x/\text{ZIS-6}$  was selected for subsequent investigation. The catalyst dosage was set to 100 mg/L for the following tests (Fig. S13). Then, the mechanism underlying the exceptional disinfection performance of  $\text{Ti}_3\text{C}_2\text{T}_x/\text{ZIS-6}$  was investigated. As shown in Fig. S14, the samples exhibited negligible effects on ARB survival in the dark. However, upon exposure to Vis-NIR light for 30 min, a significant difference was observed in the number of ARB colonies among these

samples (Fig. 6b).  $\text{Ti}_3\text{C}_2\text{T}_x$  exhibited minimal antibacterial activity due to its poor photocatalytic properties, while pristine  $\text{ZnIn}_2\text{S}_4$  showed weak bactericidal performance owing to its mild photocatalytic performance and negligible photothermal effect. In contrast,  $\text{Ti}_3\text{C}_2\text{T}_x/\text{ZIS-6}$  composite completely inactivated ARB within 25 min, which can be attributed to its higher ROS yield and better photothermal effect. Notably,  $\text{Ti}_3\text{C}_2\text{T}_x/\text{ZIS-6}$  exhibited excellent normalized sterilization efficiency (NSE) in comparison to other reported photocatalysts for water disinfection, while also exhibiting a lower synthetic cost than the majority of photocatalysts (Fig. 5c and Table S4). The sterilization



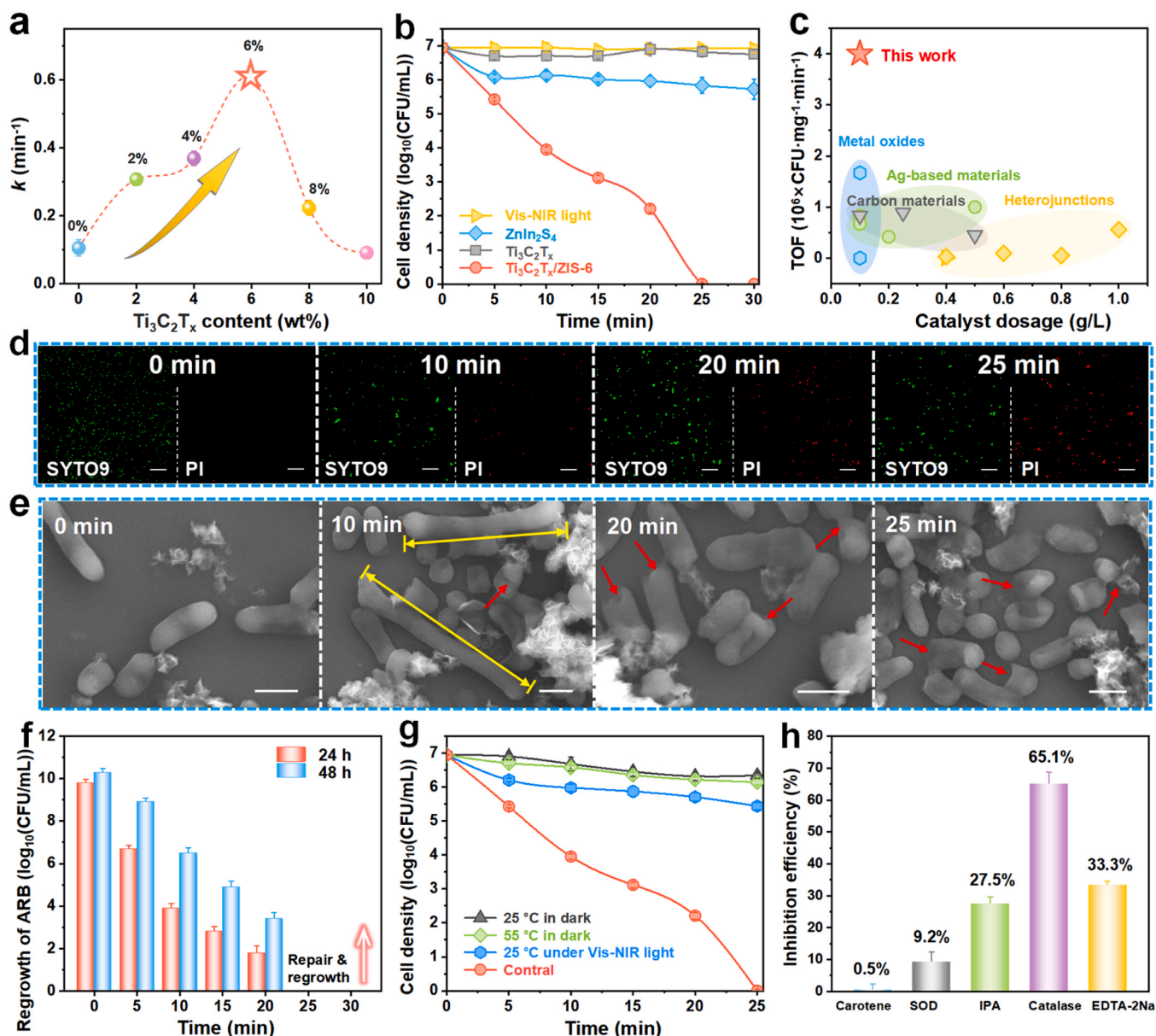


**Fig. 6.** (a) First-order rate constants ( $k$ ) for the inactivation of ARB ( $10^7$  CFU/mL) by  $\text{Ti}_3\text{C}_2\text{T}_x/\text{ZIS}$  (100 mg/L) with different  $\text{Ti}_3\text{C}_2\text{T}_x$  contents. (b) Sterilization efficiency of the prepared photocatalysts against ARB. (c) Comparison of NSE-values of the advanced catalytic materials for sterilization. (d) Confocal fluorescence images of live/dead ARB during photocatalytic inactivation. The scale bar was 10  $\mu\text{m}$ . (e) SEM of ARB at various photocatalytic treatment times with  $\text{Ti}_3\text{C}_2\text{T}_x/\text{ZIS}$ -6 present. The scale bar was 1  $\mu\text{m}$ . (f) The ARB regrew after being incubated at 37 °C for 24 and 48 h, respectively. (g) Sterilization efficiency of  $\text{Ti}_3\text{C}_2\text{T}_x/\text{ZIS}$ -6 under different conditions. (h) The inhibition efficiencies of various quenchers on the photocatalytic sterilization effect of  $\text{Ti}_3\text{C}_2\text{T}_x/\text{ZIS}$ -6.

efficiency of  $\text{Ti}_3\text{C}_2\text{T}_x/\text{ZIS}$ -6 remained superior compared to traditional water treatment technologies (Table S5). Furthermore, the photocatalytic sterilization performance of  $\text{Ti}_3\text{C}_2\text{T}_x$  in conjunction with other semiconductors was also investigated. As depicted in Fig. S15, the sterilization efficiencies of  $\text{Ti}_3\text{C}_2\text{T}_x/\text{BiOBr}$ ,  $\text{Ti}_3\text{C}_2\text{T}_x/\text{TiO}_2$  and  $\text{Ti}_3\text{C}_2\text{T}_x/\text{BiO}_2$  were found to be significantly inferior compared to that of  $\text{Ti}_3\text{C}_2\text{T}_x/\text{ZIS}$ -6.

The qualitative bacterial viability was further assessed by bacterial live/dead fluorescence staining (Fig. 6d). As the treatment time increased, an increasing amount of red fluorescence (indicating dead bacteria) was observed. After being treated with  $\text{Ti}_3\text{C}_2\text{T}_x/\text{ZIS}$ -6 for 25 min, the red and green fluorescence (representing all bacteria) exhibited significant overlap, suggesting that nearly all the bacteria were inactivated by  $\text{Ti}_3\text{C}_2\text{T}_x/\text{ZIS}$ -6 (Fig. S16). Additionally, the morphology of bacteria at various stages of photocatalytic disinfection was observed using SEM (Fig. 6e). Prior to Vis-NIR light exposure, the

ARB cells showed a regular rod-like morphology with smooth surface. After 10 min of irradiation, the membrane surface exhibited evident perforations and the cells underwent elongation to twice their original size, which could be attributed to ROS oxidation. After 25 min, complete destruction of cells occurred with some flattening due to loss of cellular contents, indicating irreversible inactivation of ARB. These findings suggest that bacteria death is initiated by membrane damage and progresses over time through the destruction of intracellular components. The results of Superoxide dismutase (SOD) and Catalase (CAT) activity in bacteria during the photocatalytic reaction indicate that the oxidation stress induced by the ROS exceeds the *E. coli*'s intrinsic defense mechanisms, resulting in extensive bacterial mortality (Fig. S17). The regrowth potential of ARB was assessed following treatment with  $\text{Ti}_3\text{C}_2\text{T}_x/\text{ZIS}$ -6 under Vis-NIR light irradiation at varying durations to prevent reactivation and regrowth during storage of the treated effluent. As exhibited in Fig. 6f, no regrowth was observed after a 25-min

treatment period, demonstrating the permanent inactivation effect of  $\text{Ti}_3\text{C}_2\text{T}_x/\text{ZIS-6}$  on ARB.

The photothermal effect plays a crucial role in enhancing the photocatalytic disinfection performance, since the elevated temperature not only facilitates the transfer of photoexcited charges and thus boosts the photocatalytic activity [45], but also modulates bacteria metabolism by altering their protein and nucleic acid activities, as well as cell wall structure and membrane function [11,47]. To evaluate the contribution of photodynamic and heating effects to the sterilization activity of the materials, we assessed the bactericidal activity of single photodynamic effect under Vis-NIR light irradiation in a water bath at a constant temperature of 25 °C, while we evaluated the bactericidal activity of single heating effect in dark in a water bath at a constant temperature of 55 °C (Fig. 6g and S18). Under single photodynamic effect alone, 1.5-log reduction of ARB was achieved after 25 min of treatment with  $\text{Ti}_3\text{C}_2\text{T}_x/\text{ZIS-6}$ . Moreover, under heating effect alone, an 0.8-log reduction of ARB can be observed (Fig. 6g). The combined photodynamic and photothermal antibacterial effects resulted in a total reduction of ARB by 2.3-log, which was less than the synergistic antibacterial effect that led to a remarkable decrease in ARB by up to 7-log. Besides, the bactericidal activity of  $\text{Ti}_3\text{C}_2\text{T}_x/\text{ZIS-6}$  remained virtually unchanged under dark conditions, regardless of whether it was subjected to thermal treatment or not, indicating that the treatment at 55 °C for 25 min was insufficient for bacterial eradication. Therefore, the photothermal synergistic effect can achieve significantly enhanced bactericidal performance compared to single photodynamic or heating effects, owing to its ability to promote the production of ROS. We have confirmed the existence of  $\text{H}_2\text{O}_2$ ,  $\bullet\text{OH}$ ,  $\text{O}_2^{\bullet-}$  and  $^1\text{O}_2$  in the photocatalytic process of  $\text{Ti}_3\text{C}_2\text{T}_x/\text{ZIS-6}$ . Therefore, chemical quenching experiments were conducted to further determine the contribution of these ROS to ARB inactivation (Fig. 6h and S19). As shown in Fig. 6h, the inhibition efficiencies of catalase ( $\text{H}_2\text{O}_2$  scavenger), EDTA-2Na ( $\text{h}^+$  scavenger), isopropanol ( $\bullet\text{OH}$  scavenger), superoxide dismutase (SOD,  $\text{O}_2^{\bullet-}$  scavenger) and carotene ( $^1\text{O}_2$  scavenger)

on the photocatalytic sterilization effect of  $\text{Ti}_3\text{C}_2\text{T}_x/\text{ZIS-6}$  reached 65.1%, 33.3%, 27.5%, 9.2% and 0.5%, respectively. Therefore,  $\text{H}_2\text{O}_2$ ,  $\bullet\text{OH}$  and  $\text{h}^+$  were the predominant species responsible for ARB inactivation (Li et al., 2021b). Moreover, the results of photocatalytic sterilization experiments using  $\text{Ti}_3\text{C}_2\text{T}_x/\text{ZIS}$  against different generations of bacteria (Fig. S20a), along with the expression analysis findings of ROS-related genes (Fig. S20b-c), demonstrated that bacteria did not develop resistance to ROS.

### 3.5. ARGs removal performance

The ARGs released from the damaged ARB can migrate steadily through various environmental media and proliferate in host microbes, posing a potential threat to public health. Therefore, it is necessary to evaluate the inactivation of ARGs during the disinfection process of  $\text{Ti}_3\text{C}_2\text{T}_x/\text{ZIS-6}$ . The nucleic acids leaked from damaged ARB cells during the photocatalytic disinfection process were detected using UV-vis spectrophotometer at 260 nm [48]. As displayed in Fig. 7a, the absorbance of nucleic acids increased with treatment time within the first 40 min and then gradually decreased, indicating that intracellular nucleic acids flowed out due to cell membrane damage and were subsequently inactivated by ROS in the system. In addition, the amplicons of *tetA*, *ampC* and *sul2* were selected as the target model to further evaluate the ARGs removal performance of  $\text{Ti}_3\text{C}_2\text{T}_x/\text{ZIS-6}$ . As shown in Fig. 7b,  $\text{Ti}_3\text{C}_2\text{T}_x/\text{ZIS-6}$  exhibited excellent removal efficiency on *tetA* under Vis-NIR irradiation, with  $\lg(\text{C}/\text{C}_0)$  values reaching  $-4.8$ , while  $\text{Ti}_3\text{C}_2\text{T}_x$  and  $\text{ZnIn}_2\text{S}_4$  showed negligible degradation effects on *tetA*. The degradation effect on ARGs was not observed in the dark for  $\text{Ti}_3\text{C}_2\text{T}_x/\text{ZIS-6}$  (Fig. S21).  $\text{Ti}_3\text{C}_2\text{T}_x/\text{ZIS-6}$  also exhibited remarkable photocatalytic degradation efficiencies towards *ampC* and *sul2*, with  $\lg(\text{C}/\text{C}_0)$  values reaching  $-4.7$  and  $-5.7$ , respectively (Fig. S22). The removal efficiency of ARGs by  $\text{Ti}_3\text{C}_2\text{T}_x/\text{ZIS-6}$  remained superior compared to traditional water treatment technologies (Table S6).

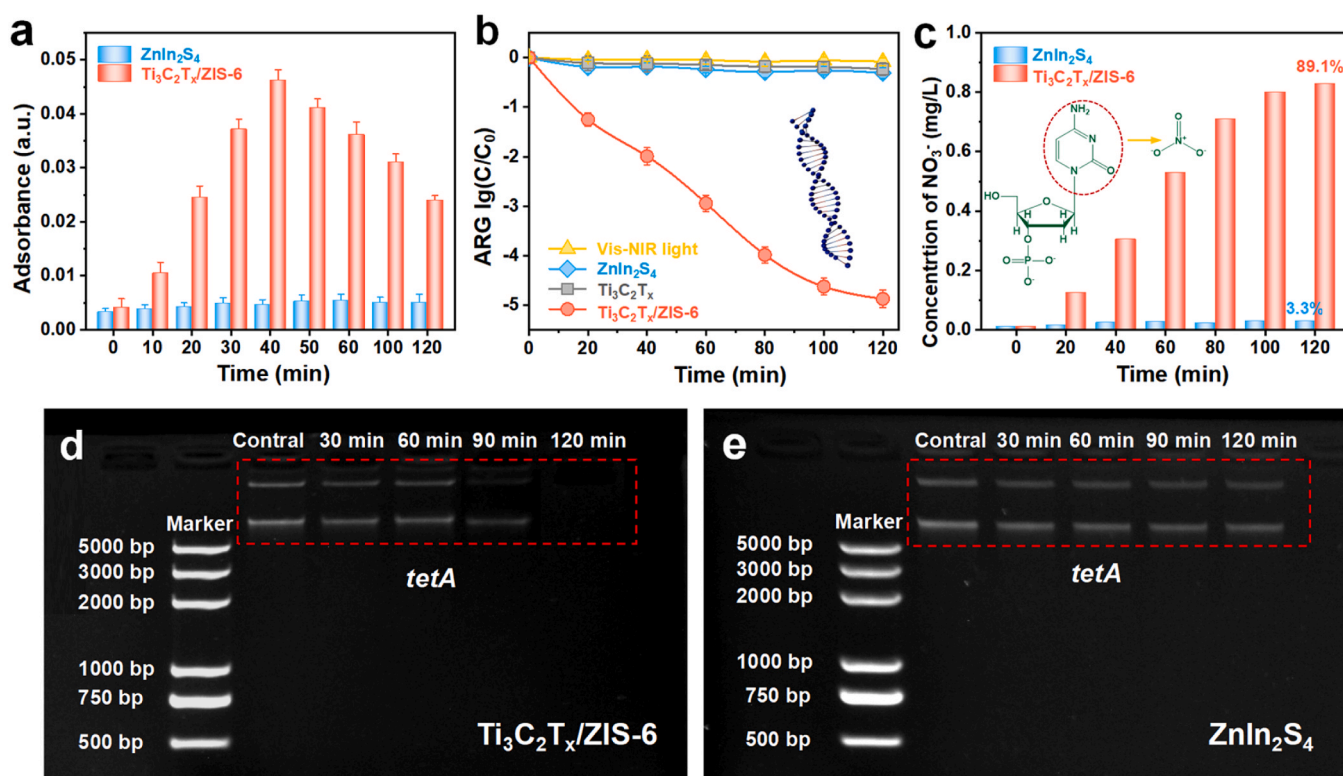


**Fig. 7.** (a) The absorbance (260 nm) of nucleic acids leaked from the damaged ARB cells during the photocatalytic disinfection process. (b) Time course of *tetA* degradation. Conditions: [Catalyst]: 100 mg/L, [*tetA*]<sub>0</sub>: ( $10^{12}$  copies/mL). (c) Concentration of  $\text{NO}_3^-$  during the *tetA* (1 mg/L) removal process. Agarose gel electrophoresis images of plasmids before and after treatment with (d)  $\text{Ti}_3\text{C}_2\text{T}_x/\text{ZIS-6}$  and (e)  $\text{ZnIn}_2\text{S}_4$ .

Although fractured or damaged extracellular ARGs exhibit lower transformation efficiency than intact ARGs, they still have the potential to diffuse genes and evolve bacteria [49–51]. Therefore, ion chromatography was employed to assess the extent of damage to ARGs induced by  $\text{Ti}_3\text{C}_2\text{T}_x/\text{ZIS-6}$ . The concentration of  $\text{NO}_3^-$  released from *tetA* (1 mg/L) reached 0.83 mg/L after 60 min treatment with  $\text{Ti}_3\text{C}_2\text{T}_x/\text{ZIS-6}$ , demonstrating that 89.1% of the nitrogen in *tetA* can be mineralized (Fig. 7c). Moreover, agarose gel electrophoresis was used to determine the chain length distribution of plasmids following treatment with catalysts. Obviously, the bright band corresponding to DNA disappeared after 120 min of treatment with  $\text{Ti}_3\text{C}_2\text{T}_x/\text{ZIS-6}$  (Fig. 7d), while it remained visible after a similar treatment with  $\text{ZnIn}_2\text{S}_4$  (Fig. 7e). The disappearance of bands treated with  $\text{Ti}_3\text{C}_2\text{T}_x/\text{ZIS-6}$  suggested that DNA amplification was not feasible [52]. High performance liquid chromatography (HPLC) was conducted to investigate the deep oxidation products of ARGs during the photocatalytic process of  $\text{Ti}_3\text{C}_2\text{T}_x/\text{ZIS-6}$ . As shown in Table S7, a range of deep oxidation products of bases and deoxyribose were detected in the treated solution, suggesting the excellent deep oxidation effect of  $\text{Ti}_3\text{C}_2\text{T}_x/\text{ZIS-6}$  on ARGs. The above-mentioned findings demonstrated the remarkable effectiveness of  $\text{Ti}_3\text{C}_2\text{T}_x/\text{ZIS-6}$  in degrading ARGs, as well as its ability to thoroughly oxidize them into minute molecules and inorganic ions without posing any potential harm.

### 3.6. The stability and anti-environment disturbance ability of $\text{Ti}_3\text{C}_2\text{T}_x/\text{ZIS}$

To assess the reusability of  $\text{Ti}_3\text{C}_2\text{T}_x/\text{ZIS}$ , five consecutive cycles of ARB inactivation experiments were carried out. The sterilization activity of  $\text{Ti}_3\text{C}_2\text{T}_x/\text{ZIS-6}$  decreased slightly after the fifth cycle (Fig. 8a), suggesting its satisfactory reusability. Furthermore, the microstructure and morphology of  $\text{Ti}_3\text{C}_2\text{T}_x/\text{ZIS-6}$  remained unchanged even after five cycles (Fig. 8b and S23), indicating the excellent stability of  $\text{Ti}_3\text{C}_2\text{T}_x/\text{ZIS}$ . To evaluate the bactericidal performance of  $\text{Ti}_3\text{C}_2\text{T}_x/\text{ZIS}$  in actual water

samples, experiments were conducted to deactivate ARB in river water (Haihe River, Tianjin, China), lake water (Horseshoe Lake, Tianjin, China) and secondary effluent (Nankai University wastewater treatment plant, Tianjin, China). The water quality data of these three water samples were listed in Table S8. As shown in Fig. 8c, the sterilization activity of  $\text{Ti}_3\text{C}_2\text{T}_x/\text{ZIS-6}$  decreased slightly in the three actual water samples, which could be attributed to the influence of pH levels and the presence of organic and inorganic anions within these samples. Based on data obtained from Table S8 regarding the quality of these water samples, we conducted further investigations into how pH values, HA (as representative natural organic matter),  $\text{HCO}_3^-$ ,  $\text{NO}_3^-$ ,  $\text{SO}_4^{2-}$  and  $\text{PO}_4^{3-}$  impacted upon the sterilization performance of  $\text{Ti}_3\text{C}_2\text{T}_x/\text{ZIS-6}$ .

As shown in Fig. 8d and S24, the sterilization efficiency of  $\text{Ti}_3\text{C}_2\text{T}_x/\text{ZIS-6}$  was slightly impeded under both acidic and alkaline conditions compared to neutral conditions. Interestingly, HA facilitated the bacterial inactivation by  $\text{Ti}_3\text{C}_2\text{T}_x/\text{ZIS-6}$ , possibly attributed to the generation of active species from photoinduced  $^3\text{HA}^{*+}$  derived from HA [8]. Moreover, the  $\text{HCO}_3^-$ ,  $\text{NO}_3^-$ ,  $\text{SO}_4^{2-}$  and  $\text{PO}_4^{3-}$  exhibited negligible impact on the disinfection property of  $\text{Ti}_3\text{C}_2\text{T}_x/\text{ZIS-6}$ . The above results indicate that  $\text{Ti}_3\text{C}_2\text{T}_x/\text{ZIS}$  exhibits exceptional stability and resistance to environmental disturbances.

### 3.7. Investigation of the wastewater treatment system

To facilitate catalyst recovery and prevent secondary pollution caused by catalyst loss,  $\text{Ti}_3\text{C}_2\text{T}_x/\text{ZIS}$  carbon felt (namely  $\text{Ti}_3\text{C}_2\text{T}_x/\text{ZIS}/\text{GF}$ ) was prepared via in-situ growth method using graphite felt (GF) as a carrier. To assess the potential application of  $\text{Ti}_3\text{C}_2\text{T}_x/\text{ZIS}$ , a continuous flow reactor consisting of  $\text{Ti}_3\text{C}_2\text{T}_x/\text{ZIS}/\text{GF}$  was employed to treat actual wastewater under simulated sunlight irradiation (Fig. 9a). The carbon felt possesses a large specific surface area and pore structure, onto which the catalyst is stably attached to ensure its retention during the reaction (Fig. 9b-d). The photocatalytic disinfection performance of  $\text{Ti}_3\text{C}_2\text{T}_x/\text{ZIS}/$

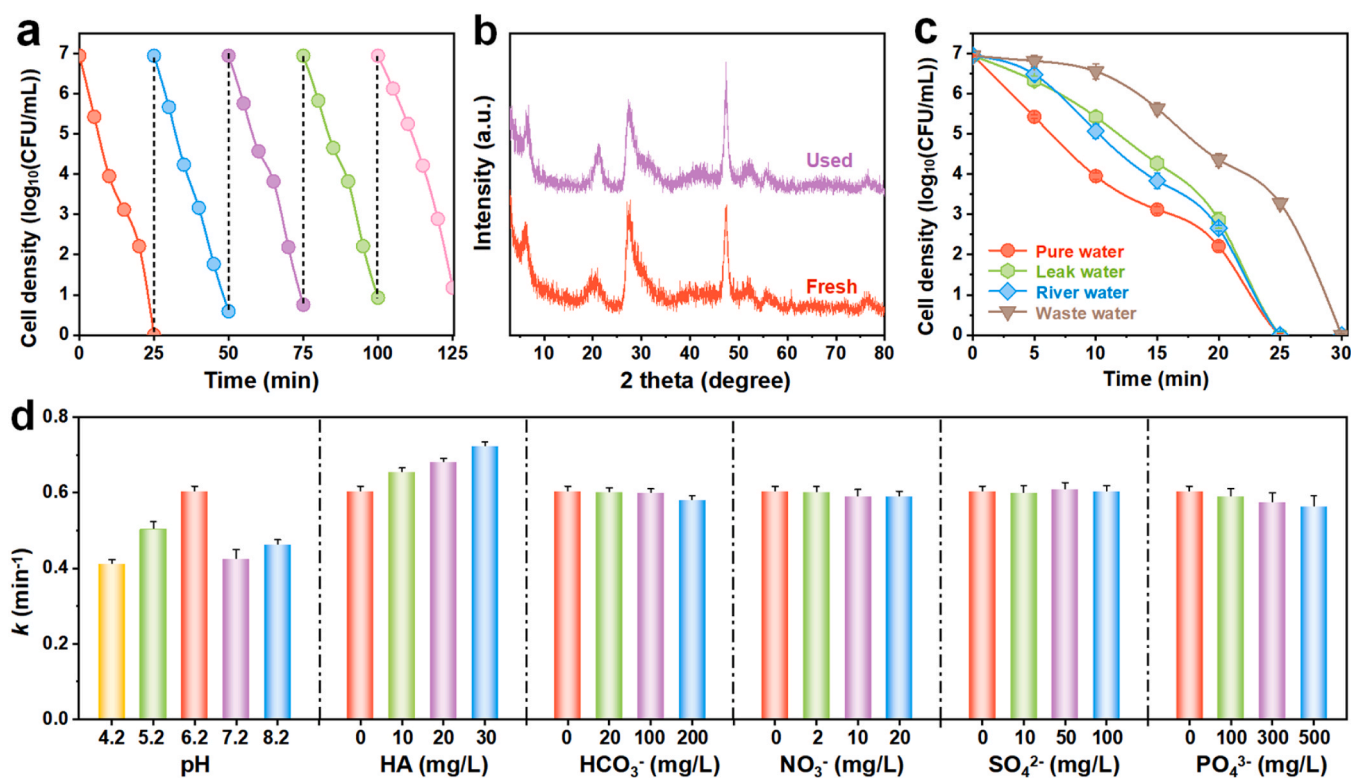


**Fig. 8.** (a) Cycling runs for ARB inactivation. (b) The XRD pattern of  $\text{Ti}_3\text{C}_2\text{T}_x/\text{ZIS-6}$  before and after five cycles. (c) Sterilization efficiency of  $\text{Ti}_3\text{C}_2\text{T}_x/\text{ZIS-6}$  in different water samples. (d) Effects of pH value, HA,  $\text{NO}_3^-$ ,  $\text{HCO}_3^-$ ,  $\text{NO}_3^-$ ,  $\text{SO}_4^{2-}$  and  $\text{PO}_4^{3-}$  on the sterilization of  $\text{Ti}_3\text{C}_2\text{T}_x/\text{ZIS-6}$ . Conditions: [Catalyst]: 100 mg/L, [ARB]<sub>0</sub>:  $10^7$  CFU/mL, [light]: Vis-NIR.



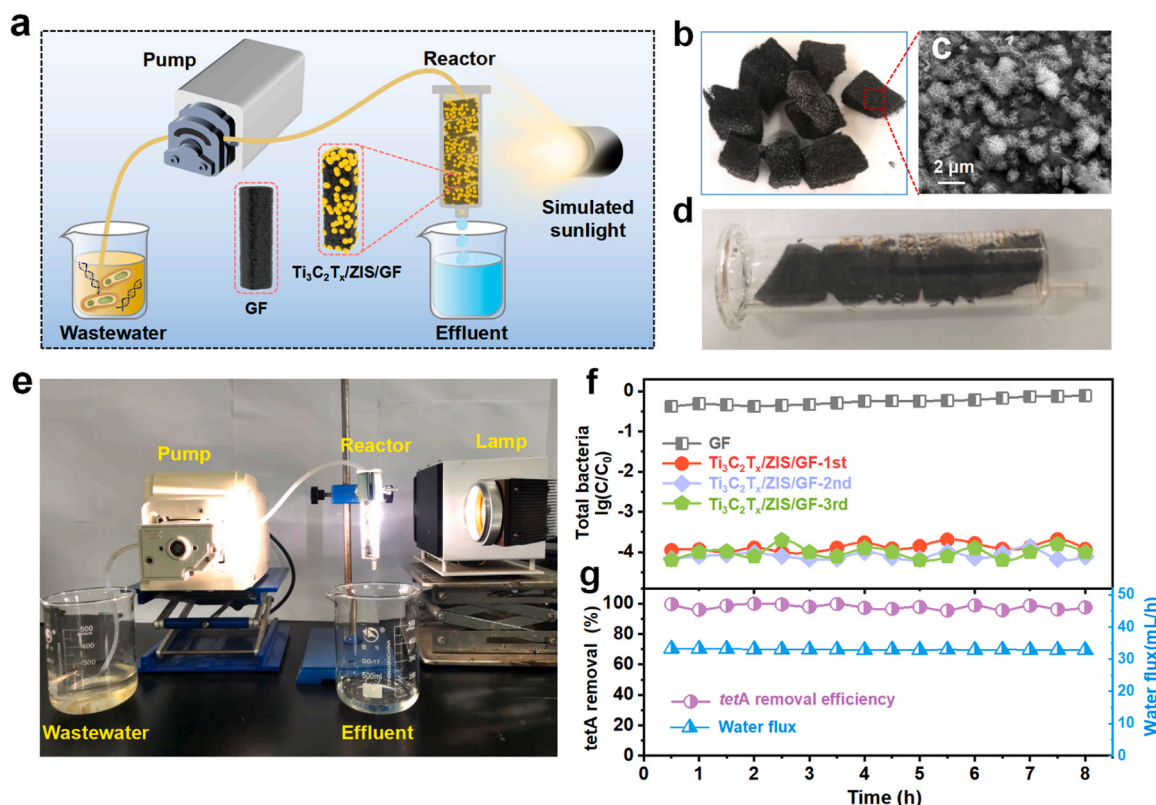


**Fig. 9.** (a) Schematic diagram of the continuous-flow reactor. (b) Photograph of the catalyst-loaded carbon felt. (c) SEM image of catalyst-loaded carbon felt surface. (d) and (e) Photograph of the experiment device. (f) Disinfection efficiency of GF and Ti<sub>3</sub>C<sub>2</sub>T<sub>x</sub>/ZIS/GF reactors. (g) ARG removal efficiency (left axis) and water flow rate (right axis) over time of treatment. Conditions: [Catalyst] = 200 mg; light source, simulated sunlight.

GF was tested using secondary effluent from Nankai University wastewater treatment plant (Tianjin, China), with an initial total bacteria density of approximately  $10^4$  CFU/mL (Fig. 9e). The Ti<sub>3</sub>C<sub>2</sub>T<sub>x</sub>/ZIS/GF reactor demonstrated continuous removal of bacteria from the wastewater without requiring catalyst cleaning after a single reaction. As depicted in Fig. 9f, the reactor achieved almost complete bacterial inactivation even after 8 h of continuous operation, meeting the discharge standards outlined by the Chinese National Standard (GB18918–2002).

After three operational cycles, there was no significant decline observed in the sterilization efficiency of Ti<sub>3</sub>C<sub>2</sub>T<sub>x</sub>/ZIS/GF reactor. This outcome attested to the exceptional catalytic activity and durability of the Ti<sub>3</sub>C<sub>2</sub>T<sub>x</sub>/ZIS/GF reactor. Furthermore, the *tetA* removal efficiency can exceed 95% (with an initial abundance of approximately  $2 \times 10^6$  copies/mL) during prolonged operation while maintaining a consistent flux rate (Fig. 9g). Furthermore, Ti<sub>3</sub>C<sub>2</sub>T<sub>x</sub>/ZIS-6 exhibited no cytotoxicity towards human embryonic kidney HEK-293 T cells, thereby indicating its environmentally benign nature. Therefore, Ti<sub>3</sub>C<sub>2</sub>T<sub>x</sub>/ZIS-6 exhibits promising potential for practical application in wastewater treatment.

Although the Ti<sub>3</sub>C<sub>2</sub>T<sub>x</sub>/ZIS/GF reactor, characterized by its straightforward operation, demonstrates efficient treatment performance for the secondary effluent, it currently lacks suitability for large-scale implementation. The primary cost associated with photocatalysis technology lies in the catalyst, yet the practical engineering applications find it challenging to afford a price of 0.0248 yuan/g (Table S4), necessitating further reduction in catalyst costs. For example, the cost of catalysts can be effectively diluted by prolonging the operational duration of the treatment facility and optimizing the dosage of catalysts. Besides, the current inlet water flow of the reactor is insufficient to meet the requirement of actual wastewater treatment, necessitating further optimization.

Additionally, in Ti<sub>3</sub>C<sub>2</sub>T<sub>x</sub>/ZIS/GF, a minute fraction of Ti<sub>3</sub>C<sub>2</sub>T<sub>x</sub>/ZIS

inevitably permeates into the interior of GF, thereby diminishing its utilization efficiency. In practical engineering applications, the integration of photocatalysis technology and membrane technology is expected to address this issue. The resolution of these concerns should be prioritized prior to the wide application of Ti<sub>3</sub>C<sub>2</sub>T<sub>x</sub>/ZIS.

#### 4. Conclusion

In this study, we designed a Schottky junction of Ti<sub>3</sub>C<sub>2</sub>T<sub>x</sub>/ZnIn<sub>2</sub>S<sub>4</sub> with a built-in electric field to inactivate ARB and ARG through the photothermal process. The experimental and theoretical calculation results demonstrated that the difference in work functions between Ti<sub>3</sub>C<sub>2</sub>T<sub>x</sub> and ZnIn<sub>2</sub>S<sub>4</sub> resulted in a contact potential difference, which drove the transfer of the photoinduced electrons from ZnIn<sub>2</sub>S<sub>4</sub> to Ti<sub>3</sub>C<sub>2</sub>T<sub>x</sub>, thus suppressing the recombination of the electron-hole pairs. Meanwhile, the photothermal heating effect induced by the LSPR of Ti<sub>3</sub>C<sub>2</sub>T<sub>x</sub> enhanced the temperature of Ti<sub>3</sub>C<sub>2</sub>T<sub>x</sub>/ZIS-6 system to about 55 °C under vis-NIR light irradiation, which further promoted the transfer of charges. Profiting from the photothermal synergistic effect, the H<sub>2</sub>O<sub>2</sub> yield of Ti<sub>3</sub>C<sub>2</sub>T<sub>x</sub>/ZIS-6 was 2.8 times higher than that of ZnIn<sub>2</sub>S<sub>4</sub>. Consequently, 7-log of ARB can be completely inactivated within 25 min and 89.1% of the nitrogen in ARG can be mineralized within 120 min. Moreover, Ti<sub>3</sub>C<sub>2</sub>T<sub>x</sub>/ZIS-6 exhibited exceptional recyclability and resistance to environmental interference. Notably, the Ti<sub>3</sub>C<sub>2</sub>T<sub>x</sub>/ZIS-6 flow-through reactor effectively inactivated bacteria and ARG in secondary effluent for a continuous 8-hour period, providing an efficient approach for applying photocatalytic and photothermal disinfection to actual wastewater.

#### CRediT authorship contribution statement

**Mingmei Li:** Methodology, Investigation, Writing - original draft,

Funding acquisition; **Kaida Zhang**: Investigation, Visualization; **Pengfei Wang**: Funding acquisition, Review & editing; **Zhiruo Zhou**: Methodology; **Fei Li**: Methodology; **Sihui Zhan**: Supervision, Funding acquisition, Writing - review & editing; **Yi Li**: Supervision, Funding acquisition, Writing - review & editing.

## Declaration of Competing Interest

The authors declare that they have no known competing financial interests or personal relationships that could have appeared to influence the work reported in this paper.

## Data Availability

Data will be made available on request.

## Acknowledgements

The authors gratefully acknowledge the financial support by the Natural Science Foundation of China as general projects (grant Nos. 22225604, 22076082 and 22176140), the Frontiers Science Center for New Organic Matter (grant No. 63181206), Haihe Laboratory of Sustainable Chemical Transformations and Tianjin Research Innovation Project for Postgraduate Students (grant No. 2021YJSB070).

## Appendix A. Supporting information

Supplementary data associated with this article can be found in the online version at doi:10.1016/j.apcatb.2023.123483.

## References

- J. Li, S. Ren, X. Qiu, S. Zhao, R. Wang, Y. Wang, Electroactive ultrafiltration membrane for simultaneous removal of antibiotic, antibiotic resistant bacteria, and antibiotic resistance genes from wastewater effluent, *Environ. Sci. Technol.* 56 (2022) 15120–15129.
- I.L. Pepper, J.P. Brooks, C.P. Gerba, Antibiotic resistant bacteria in municipal wastes: is there reason for concern? *Environ. Sci. Technol.* 52 (2018) 3949–3959.
- X. Shi, Y. Xia, W. Wei, B.-J. Ni, Accelerated spread of antibiotic resistance genes (ARGs) induced by non-antibiotic conditions: roles and mechanisms, *Water Res.* 224 (2022), 119060.
- C. Wang, D.M. Calderon, Y. Xiong, M. Alkahtani, Y.M. Bashawri, H. Al Qarni, P.-Y. Hong, Investigation of antibiotic resistance in hospital wastewater during the COVID-19 pandemic: is the initial phase of the pandemic contributing to antimicrobial resistance? *Environ. Sci. Technol.* 56 (2022) 15007–15018.
- F. Liu, Y. Hou, S. Wang, Z. Li, B. Zhang, M. Tong, Periodate activation by pyrite for the disinfection of antibiotic-resistant bacteria: Performance and mechanisms, *Water Res.* 230 (2023), 119508.
- R. Li, T. Chen, J. Lu, H. Hu, H. Zheng, P. Zhu, X. Pan, Metal-organic frameworks doped with metal ions for efficient sterilization: enhanced photocatalytic activity and photothermal effect, *Water Res.* 229 (2023), 119366.
- X. Chen, Z. Wang, X. Shen, Y. Zhang, Y. Lou, C. Pan, Y. Zhu, J. Xu, A plasmonic Z-scheme Ag@AgCl/PDI photocatalyst for the efficient elimination of organic pollutants, antibiotic resistant bacteria and antibiotic resistance genes, *Appl. Catal. B Environ.* 324 (2023), 122220.
- M. Li, P. Wang, Z. Ji, Z. Zhou, Y. Xia, Y. Li, S. Zhan, Efficient photocatalytic oxygen activation by oxygen-vacancy-rich CeO<sub>2</sub>-based heterojunctions: synergistic effect of photoexcited electrons transfer and oxygen chemisorption, *Appl. Catal. B Environ.* 289 (2021), 120020.
- R. Zhang, C. Song, M. Kou, P. Yin, X. Jin, L. Wang, Y. Deng, B. Wang, D. Xia, P. K. Wong, L. Ye, Sterilization of *Escherichia coli* by photothermal synergy of WO<sub>3-x</sub>/C nanosheet under infrared light irradiation, *Environ. Sci. Technol.* 54 (2020) 3691–3701.
- X. Jin, Y.-H. Xiong, X.-Y. Zhang, R. Wang, Y. Xing, S. Duan, D. Chen, W. Tian, F.-J. Xu, Self-adaptive antibacterial porous implants with sustainable responses for infected bone defect therapy, *Adv. Funct. Mater.* 29 (2019) 18079.
- J. Li, Z. Li, X. Liu, C. Li, Y. Zheng, K.W.K. Yeung, Z. Cui, Y. Liang, S. Zhu, W. Hu, Y. Qi, T. Zhang, X. Wang, S. Wu, Interfacial engineering of Bi<sub>2</sub>S<sub>3</sub>/Ti<sub>3</sub>C<sub>2</sub>T<sub>x</sub> MXene based on work function for rapid photo-excited bacteria-killing, *Nat. Commun.* 12 (2021) 1224.
- A.T. Spinks, R.H. Dunstan, T. Harrison, P. Coombes, G. Kucera, Thermal inactivation of water-borne pathogenic and indicator bacteria at sub-boiling temperatures, *Water Res.* 40 (2006) 1326–1332.
- Z. Tang, D. Ma, Q. Chen, Y. Wang, M. Sun, Q. Lian, J. Shang, P.K. Wong, C. He, D. Xia, T. Wang, Nanomaterial-enabled photothermal-based solar water disinfection processes: fundamentals, recent advances, and mechanisms, *J. Hazard. Mater.* 437 (2022), 129373.
- S. Loeb, C. Li, J.-H. Kim, Solar Photothermal disinfection using broadband-light absorbing gold nanoparticles and carbon black, *Environ. Sci. Technol.* 52 (2018) 205–213.
- D. Xia, H. Liu, B. Xu, Y. Wang, Y. Liao, Y. Huang, L. Ye, C. He, P.K. Wong, R. Qiu, Single Ag atom engineered 3D-MnO<sub>2</sub> porous hollow microspheres for rapid photothermocatalytic inactivation of *E. coli* under solar light, *Appl. Catal. B Environ.* 245 (2019) 177–189.
- X. Cheng, R. Sun, L. Yin, Z. Chai, H. Shi, M. Gao, Light-triggered assembly of gold nanoparticles for photothermal therapy and photoacoustic imaging of tumors in vivo, *Adv. Mater.* 29 (2017) 1604894.
- R.C. Elias, S. Linic, Elucidating the roles of local and nonlocal rate enhancement mechanisms in plasmonic catalysis, *J. Am. Chem. Soc.* 144 (2022) 19990–19998.
- J.-W. Xu, K. Yao, Z.-K. Xu, Nanomaterials with a photothermal effect for antibacterial activities: an overview, *Nanoscale* 11 (2019) 8680–8691.
- H. Lin, X. Wang, L. Yu, Y. Chen, J. Shi, Two-dimensional ultrathin MXene ceramic nanosheets for photothermal conversion, *Nano Lett.* 17 (2017) 384–391.
- X. Wu, J. Wang, Z. Wang, F. Sun, Y. Liu, K. Wu, X. Meng, J. Qiu, Boosting the electrocatalysis of MXenes by plasmon-induced thermalization and hot-electron injection, *Angew. Chem. Int. Ed.* 60 (2021) 9416–9420.
- D.B. Velusamy, J.K. El-Demellawi, A.M. El-Zohry, A. Giugni, S. Lopatin, M. N. Hedhili, A.E. Mansour, E. Di Fabrizio, O.F. Mohammed, H.N. Alshareef, MXenes for plasmonic photodetection, *Adv. Mater.* 31 (2019) 1807658.
- F. Shahzad, A. Iqbal, H. Kim, C.M. Koo, 2D transition metal carbides (MXenes): applications as an electrically conducting material, *Adv. Mater.* 32 (2020) 2002159.
- W. Zhang, Y. Chen, G. Zhang, X. Tan, Q. Ji, Z. Wang, H. Liu, J. Qu, Hot-electron-induced photothermal catalysis for energy-dependent molecular oxygen activation, *Angew. Chem. Int. Ed.* 60 (2021) 4872–4878.
- W. Fan, J. Cui, Q. Li, Y. Huo, D. Xiao, X. Yang, H. Yu, C. Wang, P. Jarvis, T. Lyu, M. Huo, Bactericidal efficiency and photochemical mechanisms of micro/nano bubble-enhanced visible light photocatalytic water disinfection, *Water Res.* 203 (2021), 117531.
- Y. Feng, L. Dai, Z. Wang, Y. Peng, E. Duan, Y. Liu, L. Jing, X. Wang, A. Rastegarpanah, H. Dai, J. Deng, Photothermal synergistic effect of Pt<sub>1</sub>/CuO-CeO<sub>2</sub> single-atom catalysts significantly improving toluene removal, *Environ. Sci. Technol.* 56 (2022) 8722–8732.
- D. Fan, Y. Lu, H. Zhang, H. Xu, C. Lu, Y. Tang, X. Yang, Synergy of photocatalysis and photothermal effect in integrated 0D perovskite oxide/2D MXene heterostructures for simultaneous water purification and solar steam generation, *Appl. Catal. B Environ.* 295 (2021), 120285.
- X. Wu, G. Chen, L. Li, J. Wang, G. Wang, ZnIn<sub>2</sub>S<sub>4</sub>-based S-scheme heterojunction photocatalyst, *J. Mater. Sci. Technol.* 167 (2023) 184–204.
- F. Xing, C. Cheng, J. Zhang, Q. Liu, C. Chen, C. Huang, Tunable charge transfer efficiency in HxMoO<sub>3</sub>@ZnIn<sub>2</sub>S<sub>4</sub> hierarchical direct Z-scheme heterojunction toward efficient visible-light-driven hydrogen evolution, *Appl. Catal. B Environ.* 285 (2021), 119818.
- H. Zhan, R. Zhou, P. Wang, Q. Zhou, Selective hydroxyl generation for efficient pollutant degradation by electronic structure modulation at Fe sites, *Proc. Natl. Acad. Sci. U. S. A.* 120 (2023), e2305378120.
- M. Li, P. Wang, K. Zhang, H. Zhang, Y. Bao, Y. Li, S. Zhan, J.C. Crittenden, Single cobalt atoms anchored on Ti<sub>3</sub>C<sub>2</sub>T<sub>x</sub> with dual reaction sites for efficient adsorption-degradation of antibiotic resistance genes, *Proc. Natl. Acad. Sci. U. S. A.* 120 (2023), e2305705120.
- J. Hafner, Ab-initio simulations of materials using VASP: Density-functional theory and beyond, *J. Comput. Chem.* 29 (2008) 2044–2078.
- P.E. Blöchl, Projector augmented-wave method, *Phys. Rev. B* 50 (1994) 17953–17979.
- J.P. Perdew, K. Burke, M. Ernzerhof, Generalized gradient approximation made simple, *Phys. Rev. Lett.* 77 (1996) 3865–3868.
- S. Grimme, Semiempirical GGA-type density functional constructed with a long-range dispersion correction, *J. Comput. Chem.* 27 (2006) 1787–1799.
- T. Ogitsu, E. Schwegler, F. Gygi, G. Galli, Melting of Lithium Hydride under Pressure, *Phys. Rev. Lett.* 91 (2003), 175502.
- V. Wang, N. Xu, J.-C. Liu, G. Tang, W.-T. Geng, VASPKIT: a user-friendly interface facilitating high-throughput computing and analysis using VASP code, *Comput. Phys. Commun.* 267 (2021), 108033.
- G. Zuo, Y. Wang, W.L. Teo, A. Xie, Y. Guo, Y. Dai, W. Zhou, D. Jana, Q. Xian, W. Dong, Y. Zhao, Ultrathin ZnIn<sub>2</sub>S<sub>4</sub> nanosheets anchored on Ti<sub>3</sub>C<sub>2</sub>T<sub>x</sub> MXene for photocatalytic H<sub>2</sub> evolution, *Angew. Chem. Int. Ed.* 59 (2020) 11287–11292.
- M. Ghidoui, M.R. Lukatskaya, M.-Q. Zhao, Y. Gogotsi, M.W. Barsoum, Conductive two-dimensional titanium carbide 'clay' with high volumetric capacitance, *Nature* 516 (2014) 78–81.
- C. Li, Y. Liu, Z. Zhuo, H. Ju, D. Li, Y. Guo, X. Wu, H. Li, T. Zhai, Local charge distribution engineered by Schottky heterojunctions toward urea electrolysis, *Adv. Energy Mater.* 8 (2018) 1801775.
- M.-Q. Yang, Y.-J. Xu, W. Lu, K. Zeng, H. Zhu, Q.-H. Xu, G.W. Ho, Self-surface charge exfoliation and electrostatically coordinated 2D hetero-layered hybrids, *Nat. Commun.* 8 (2017) 14224.
- T.-F. Yeh, C.-Y. Teng, S.-J. Chen, H. Teng, Nitrogen-doped graphene oxide quantum dots as photocatalysts for overall water-splitting under visible light illumination, *Adv. Mater.* 26 (2014) 3297–3303.
- M.J. Bierman, S. Jin, Potential applications of hierarchical branching nanowires in solar energy conversion, *Energy Environ. Sci.* 2 (2009) 1050–1059.

- [43] G. Dong, D.L. Jacobs, L. Zang, C. Wang, Carbon vacancy regulated photoreduction of NO to N<sub>2</sub> over ultrathin g-C<sub>3</sub>N<sub>4</sub> nanosheets, *Appl. Catal. B Environ.* 218 (2017) 515–524.
- [44] M. Li, D. Li, Z. Zhou, P. Wang, X. Mi, Y. Xia, H. Wang, S. Zhan, Y. Li, L. Li, Plasmonic Ag as electron-transfer mediators in Bi<sub>2</sub>MoO<sub>6</sub>/Ag-AgCl for efficient photocatalytic inactivation of bacteria, *Chem. Eng. J.* 382 (2020), 122762.
- [45] L. Jing, M. Xie, Y. Xu, C. Tong, H. Zhao, N. Zhong, H. Li, I.D. Gates, J. Hu, Multifunctional 3D MoS<sub>x</sub>/Zn<sub>3</sub>In<sub>2</sub>S<sub>6</sub> nanoflower for selective photothermal-catalytic biomass oxidative and non-selective organic pollutants degradation, *Appl. Catal. B Environ.* 318 (2022), 121814.
- [46] S. Rajput, M.X. Chen, Y. Liu, Y.Y. Li, M. Weinert, L. Li, Spatial fluctuations in barrier height at the graphene-silicon carbide Schottky junction, *Nat. Commun.* 4 (2013) 2752.
- [47] Y. Yang, L. Ma, C. Cheng, Y. Deng, J. Huang, X. Fan, C. Nie, W. Zhao, C. Zhao, Nonchemotherapeutic and robust dual-responsive nanoagents with on-demand bacterial trapping, ablation, and release for efficient wound disinfection, *Adv. Funct. Mater.* 28 (2018) 1705708.
- [48] T.-X. Yang, L.-Q. Zhao, J. Wang, G.-L. Song, H.-M. Liu, H. Cheng, Z. Yang, Improving whole-cell biocatalysis by addition of deep eutectic solvents and natural deep eutectic solvents, *ACS Sustain. Chem. Eng.* 5 (2017) 5713–5722.
- [49] X. Zhang, J. Li, M.-C. Yao, W.-Y. Fan, C.-W. Yang, L. Yuan, G.-P. Sheng, Unrecognized contributions of dissolved organic matter inducing photodamages to the decay of extracellular DNA in waters, *Environ. Sci. Technol.* 54 (2020) 1614–1622.
- [50] D.J. Levy-Booth, R.G. Campbell, R.H. Gulden, M.M. Hart, J.R. Powell, J. N. Klironomos, K.P. Pauls, C.J. Swanton, J.T. Trevors, K.E. Dunfield, Cycling of extracellular DNA in the soil environment, *Soil Biol. Biochem.* 39 (2007) 2977–2991.
- [51] K.M. Nielsen, P.J. Johnsen, D. Bensasson, D. Daffonchio, Release and persistence of extracellular DNA in the environment, *Environ. Biosaf. Res.* 6 (2007) 37–53.
- [52] X. Dong, B. Ren, Z. Sun, C. Li, X. Zhang, M. Kong, S. Zheng, D.D. Dionysiou, Monodispersed CuFe<sub>2</sub>O<sub>4</sub> nanoparticles anchored on natural kaolinite as highly efficient peroxymonosulfate catalyst for bisphenol A degradation, *Appl. Catal. B Environ.* 253 (2019) 206–217.